Landslides (2021) 18:1981–2000
DOI 10.1007/s10346-021-01639-z
Received: 3 September 2020
Accepted: 29 January 2021
Published online: 8 February 2021
© Springer-Verlag GmbH Germany part of Springer Nature 2021

Sylvain Fiolleau · Denis Jongmans · Gregory Bièvre · Guillaume Chambon · Pascal Lacroix · Agnès Helmstetter · Marc Wathelet · Michel Demierre

Multi-method investigation of mass transfer mechanisms in a retrogressive clayey landslide (Harmalière, French Alps)

Abstract The mass transfer mechanisms in landslides are complex to monitor because of their suddenness and spatial coverage. The active clayey Harmalière landslide, located 30 km south of Grenoble in the French Alps, exhibits two types of behavior: in its upper part, decameter-sized clay blocks slide along a listric slip surface, while a flow-like mechanism is observed in a clayey remolded material a few hundred meters below the headscarp. The landslide underwent a major retrogression affecting 45 ha in March 1981 and has experienced multiple reactivations since then. The last major event took place on the 26th of June 2016, and a large investigation survey was conducted to better understand the reactivation mechanism. A multi-method investigation was carried out at different temporal and spatial scales, including aerial photograph and light detection and ranging processing, correlation of optical satellite images, global navigation satellite system monitoring, continuous seismic monitoring, and passive seismic survey. The morphological evolution of the landslide was traced over the last 70 years, showing a headscarp retrogression of 700 m during multiple reactivations and a total mass transfer of more than 6×10^6 m^3. The detailed study of the 2016 event allowed to track and understand the mechanism of a mass transfer of 1×10^6 m^3 in 5 weeks, from a sliding mechanism at the headscarp to an earthflow at the toe.

Keywords Clayey landslide · Headscarp · Retrogression

Introduction

Retrogressive landslides are observed all over the world and represent a double threat to human settlements and activities by upslope retrogression of the headscarp and downslope movement of materials (e.g., Gregersen 1981; Rokoengen et al. 2001; Pagano et al. 2010; Demers et al. 2014; Zerathe et al. 2016; Lacroix et al. 2019). Most of the retrogressive failures have been reported in clay-rich formations and, particularly, in sensitive clays where the retrogression and runout distances have been thoroughly studied for hazard assessment (Locat et al. 2008; L'Heureux 2012; Turmel et al. 2018). However, retrogressive failures may also occur in granular materials (Hungr et al. 2014). In a large landslide affecting dry granular material in Peru, Lacroix et al. (2019) recently showed a self-entrainment process where the headscarp retrogression supplies material to the downslope landslide that in turn accelerates with the increasing stress and then destabilizes again the headscarp by removing the support at its base. In another climatic context, in periglacial regions, retrogressive thaw collapse has increased dramatically due to global warming and is becoming an important slope process in ice-rich permafrost terrain that could cause major problems in the near future (Wang et al. 2009; Luo et al. 2019).

In clay slopes, Hungr et al. (2014) mentioned two main retrogressive mechanisms: (1) flowslides in sensitive clays, associated to multiple rotational slides, and (2) spreading where instabilities are controlled by a weak basal surface. In the first mechanism, sliding at the headscarp produces clay remolding with increase in void ratio, moisture content, and loss in strength. As the remolded clay flows from the top to the bottom, it creates a crater and removes the mechanical support at the base of the headscarp, resulting in subsequent retrogressive slides. In spreading, the extension and dislocation of the soil mass above the slip surface forms horsts and grabens that subside in the underlying weak layer (Carson 1977; Cruden and Varnes 1996). In their inventory of 108 large retrogressive landslides in sensitive marine clays (quick clays) in the Province of Québec (Canada), Demers et al. (2014) pointed out that 58% of landslides were flowslides, 37% were spreads, and the rest 5% were other types, including a mix of the first two types. They found retrogression distances in the range of 30 to 560 m for flowslides and 40 to 1340 m for spreads. A similar study conducted in Norway (L'Heureux 2012) on 37 well-documented quick clay landslides found retrogression distances between a few tens of meters and 2000 m. However, retrogressive landslides may affect clay layers in other geomorphological settings than the sensitive marine deposits of eastern Canada and Scandinavia, with types of movement like flowslides, spreads, and also earthflows. Landslides with headscarp retrogression were reported in the Apennines (Comegna et al. 2007; Giordan et al. 2013; Bertello et al. 2018; Coltorti and Tognaccini 2019), in the Alps (Van Asch et al. 1984; Mainsant et al. 2012; Travelletti et al. 2013; Lacroix et al. 2018), in the Andes (Zerathe et al. 2016), and also in low-elevation areas such as the quick clays on the eastern coasts of the Baltic Sea (Kohv et al. 2009) or the hills of North Yorkshire, UK (Gunn et al. 2013). These landslides have developed in clay-rich geological formations of various ages (from Secondary to Quaternary) and were subject to reactivations causing failure and retrogression of the headscarp. The retrogression distance during reactivation varies between a few meters (Comegna et al. 2007) to 20–30 m during major events (Bertello et al. 2018; Lacroix et al. 2018), much less than the instantaneous retrogression observed in quick clays, which may reach 150 m (Gregersen 1981). The documented retrogression rates over a few tens of years vary between 1 m/year (van Asch et al. 2009) and 8 m/year (Travelletti et al. 2013; Zerathe et al. 2016) with intermediate values (4 m/year; Giordan et al. (2013)).

However, all landslides developing in clay-rich formations do not exhibit retrogression (Baum et al. 1998; Corominas et al. 2005; Bièvre et al. 2011; Mackey and Roering 2011). According to Tavenas et al. (1983), the retrogression mechanism requires several conditions to be active. First, the clay sliding at the headscarp has to be significantly remolded. Second, when remolded, the clay has to

have the capacity to flow out of the landslide crater. Third, the topography and geological structure must be able to evacuate the remolded clay. A key point to assess retrogression distance and rate is to understand the mass transfers between the headscarp failure (source), the downslope movement of the mass (conveyor belt), and the erosion at the toe (sink). These complex and intricated mechanisms, which can lead to a self-entrainment process under certain conditions, are still poorly known and, to our knowledge, have been little documented.

The objective of this paper is to document and quantify the mass transfer in the retrogressive Harmalière landslide (French Western Alps). This clayey landslide has shown a continuous activity since the 1950s, with a major event creating a significant headscarp in 1981 and a recent significant reactivation in 2016 (30-m-long retrogression of the headscarp). A new investigation campaign involving geological observations, seismic noise array (Wathelet et al. 2008; Pazzi et al. 2019), and LiDAR (Jaboyedoff et al. 2012) was conducted after the late June 2016 event to better constrain the morphology and geological structure of the landslide. The 60 years long landslide history, heterogeneously documented by aerial photos, remote sensing data, geological and geodetic observations, and geophysical studies, was used to quantify the magnitude and kinematics of headscarp retrogression and downslope mass flow. A conceptual model of the retrogression-evacuation cycle is proposed at the end of the paper.

The Harmalière landslide

The Harmalière landslide is located 30 km south of the city of Grenoble, France, in the Trièves area (Fig. 1). This area is affected by numerous landslides developing in a thick clayey glaciolacustrine layer (Monjuvent 1973; Giraud et al. 1991; Bièvre et al. 2011). These clayey layers date back to the Last Glacial Maximum, around 40–50 ka before present (BP), when the southward-moving Romanche glacier dammed the rivers flowing from the south and created a lake that lasted several thousand years (Monjuvent 1973). The Harmalière landslide is located at the tongue of the former glacier. The different episodes of glacier retreat and advance induced an alternating deposition of glaciolacustrine-laminated clays and of glaciolacustrine clays mixed with till (with striated pebbles up to several tens of cm in diameter). A layer of terminal moraine, with a thickness of around 50 m on the Sinard plateau to the west of the study site, caps the glaciolacustrine sequence. After glacier melting, rivers cut deeply into these geological formations, allowing the initiation of numerous landslides.

The 1450-m-long Harmalière landslide (Fig. 1) affects an area of around 1.8 x 10^6 m^2, with an estimated volume of 25 × 10^6 m^3 and a mean slope of 9° (Carrière et al. 2018). The current active area is a central strip 400 m wide at the top, narrowing to 150 m at the toe. Below the headscarp, the upper part exhibits numerous internal scarps from a few m to 20 m high with a concave shape (highlighted in light blue in Fig. 1), characteristic of a brittle behavior. In contrast, the lower part of the landslide shows a smoother morphology with the presence of a few m thick ridges. These ridges have a convex shape (yellow lines in Fig. 1) and highlight the presence of numerous slip surfaces daylighting at the landslide toe, which suggest a flow-like mechanism, as described by Hungr et al. (2014). The middle part of the landslide shows a smooth morphology with a mix of concave and convex shapes, characterizing a transition zone from solid to flow-like behavior. In this zone, a hydrographic system internal to the landslide (thin blue lines) is fed by a mid-slope depression zone accumulating water (shaded purple). According to the classification proposed by Hungr et al. (2014), the Harmalière landslide is a clay compound slide in its upper part, exhibiting back-tilted blocks (Fig. 2, photo from February 3, 2017) and horst-and-graben structures, and an earthflow with smooth morphology (Fig. 2, photo from April 28, 2018), and a flow-like pattern in its lower part. The landslide toe reaches the Monteynard artificial lake at an elevation of around 480 m. The lake results from the damming of the Drac River in 1963. As will be shown in section 3, the Harmalière landslide has retrogressed by several hundred meters over the last 50 years. In March 1981, a major landslide induced a retrogression of 500 m. It affected an area of 45 × 10^4 m^2 (Moulin and Robert 2004) and generated a mudflow at the toe (Besson 1996). On June 27, 2016, after having undergone small retrogressions (5 m in total) during 2 days, the headscarp suddenly retrogressed by about 50 m with an estimated depleted volume of more than 2 × 10^6 m^3 (Lacroix et al. 2018). This major reactivation was followed by two smaller events on January 29, 2017, and January 13, 2018.

In contrast, the contiguous Avignonet landslide (Fig. 1), which affects the same materials (quaternary glaciolacustrine clays) and is subject to the same meteorological conditions, has moved little over the same period (few centimeters). This difference in behavior can be explained by the irregular topography of the bedrock and the presence of a bulge at the toe of the Avignonet landslide, preventing mass movement at depth (Bièvre et al. 2011). The absence of such a bulge below the Harmalière landslide allows the evacuation of the remolded clay into the lake and the observed retrogressive mechanism. The lower part of the Harmalière landslide is covered with dense and thorny vegetation, which makes access and investigations in this area highly difficult (Fig. 2).

Contrary to the neighboring Avignonet landslide, no geophysical investigation was carried out prior to this study to determine the depth of the slip surfaces for the Harmalière landslide. This can be explained by the very difficult access to the landslide body and the absence of short- to mid-term risk issues. Back analyses based on mechanical data suggested a maximum depth of around 45 m for the deepest slip surface (Al Hayari et al. 1990), which is in agreement with the geotechnical and geophysical prospecting made on other landslides in the Trièves area (van Asch et al. 2009; Jongmans et al. 2009). In particular, several shear-wave velocity (Vs) measurement methods (S-wave refraction, analysis of surface waves, seismic noise techniques) on the Avignonet landslide, calibrated with boreholes, showed significant vertical vs contrasts at the level of the detected slip surfaces (Jongmans et al. 2009; Renalier et al. 2010; Bièvre et al. 2012).

Methods

A multi-technique approach was performed to establish the landslide history over the period 1948–2019. It comprises aerial photo analysis, passive seismic investigation, correlation of optical satellite images, global navigation satellite system (GNSS) measurements, and light detection and ranging (LiDAR) acquisitions. This approach was used to characterize the landslide structure, study its morphological evolution, and quantify its kinematics.

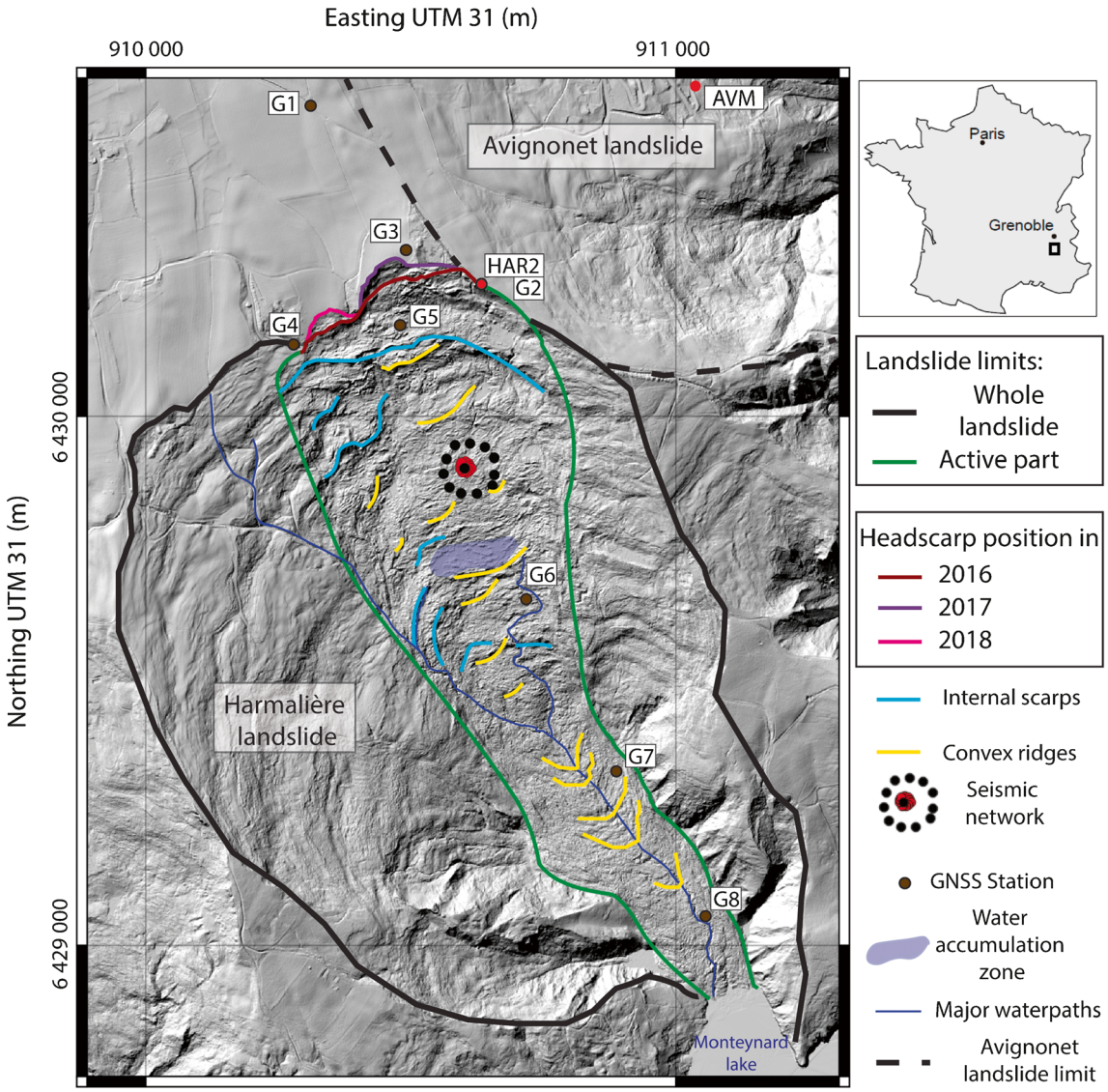

Fig. 1 Location and delineation of the Harmalière landslide on the 2019 LiDAR hillshade. The whole landslide and the present-day active part are delineated by black and green lines, respectively. The upper part is an earthslide characterized by internal scarps (> 5 m high) with a concave shape (light blue lines), while the lower part is mainly an earthflow showing convex ridges (yellow lines). Successive headscarp positions after reactivations in June 2016, January 2017, and January 2018 are shown. The location of the 100-m- and 20-m-diameter seismic arrays is indicated by black and red circles, respectively. Seismic stations HAR2 and AVM are indicated by red dots. GNSS stations (G1 to G8) are indicated by brown dots, except for G2 which is at the same location as HAR2

Aerial photographs

The Harmalière landslide activity over the last 70 years can be deduced from aerial photographs and observations described in the literature (Besson 1996; Moulin and Robert 2004; Fernandez and Whitworth 2016). Although the acquisition of aerial photos is discontinuous, they can be used to reconstruct the location of the main scarps as a function of time. In this work, previous studies are consolidated and supplemented with a longer time series. Five pairs of scanned aerial photographs provided by the French Geographic Institute (IGN) were used to reconstruct the history of the landslide from 1948 to 2003. The pictures have an average resolution of about 40–60 cm/px. They were orthorectified with the Photoscan software (www.agisoft.com), using an average of 10 ground control points (GCP). Aerial photographs acquired during the 2016 LiDAR flight (see below) with a resolution of 10 cm/px were used to complete the series.

Seismic monitoring

Continuous records from two existing seismic stations were processed to detect landquakes produced by the nearby landslide activity (Helmstetter and Garambois 2010). The first station (AVM in Fig. 1) belongs to the French permanent observatory on landslides OMIV (RESIF/OMIV 2006), while the second (HAR2 in Fig. 1) was installed on July 22, 2016, at the rear of the headscarp. Both stations acquire data with a 125 Hz sampling frequency. The station AVM is also equipped with a meteorological station.

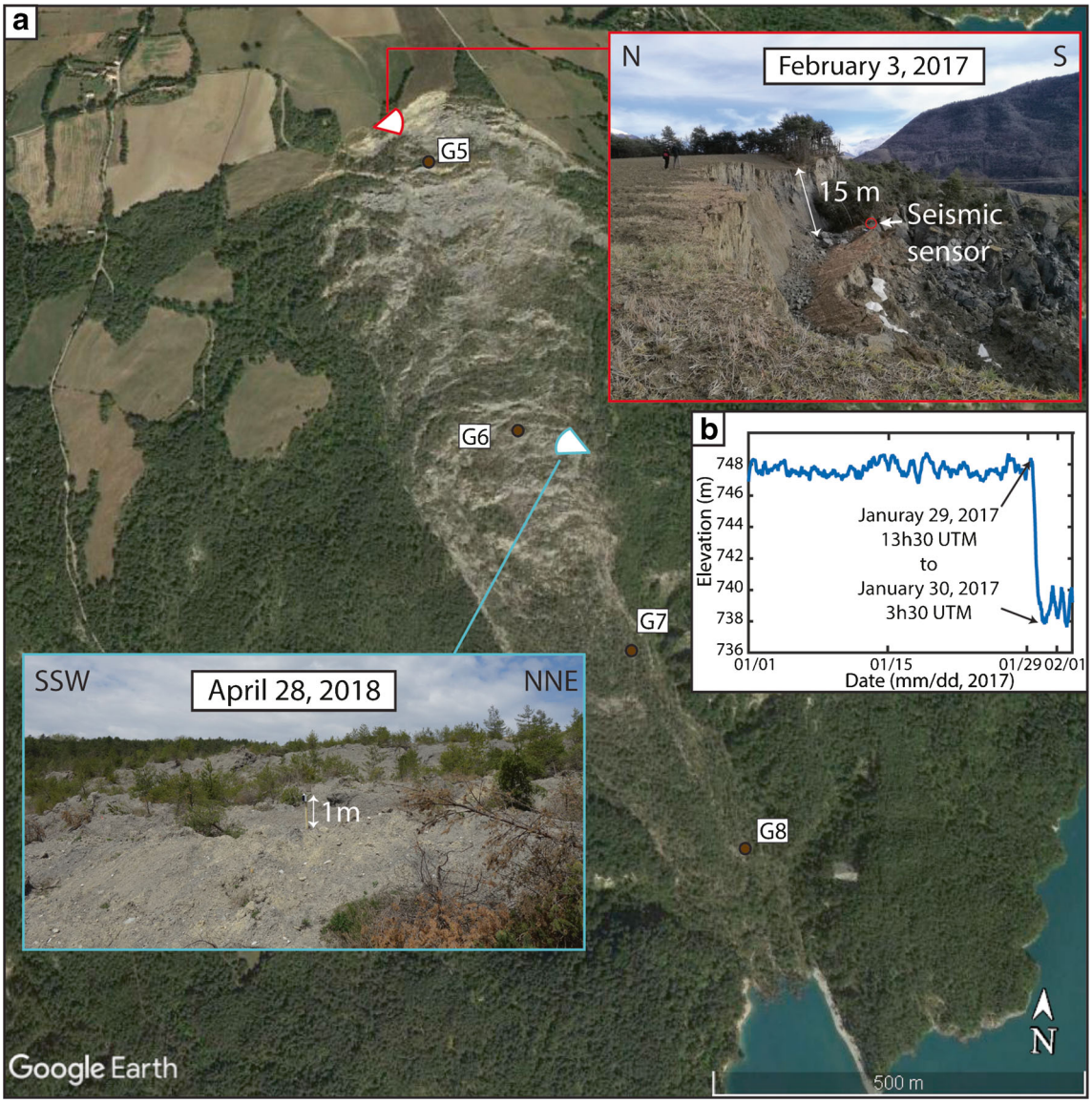

Fig. 2 **a** Google Earth view of the Harmalière landslide on 23 September 2018, with photographs of the headscarp and tilted block after the 2017 reactivation event (upper right), and of the middle zone of the landslide (lower left). The sites where the photographs were shot are shown with eye-pictogram indicating the point of view. **b** Time series of the GPS integrated in the seismic sensor (shown in the photograph on the top right) during January 29, 2017, reactivation

First, a detection method based on the amplitude of the signal at one station was applied (Helmstetter and Garambois, 2010). Then, events were grouped into clusters, and each cluster was classified as either noise or landquakes, based on the frequency content of the seismic signal and on daily fluctuations of the rate of events. A template-matching method was used to detect landquakes, using the average signal of each cluster as template. The method consists of continuously scanning data to search for signals that match a template signal with a correlation coefficient larger than a given threshold (Gibbons and Ringdal 2006). This technique has been successfully applied to detect microseismic events on glaciers (Helmstetter et al. 2015) and landslides (Yamada et al. 2016; Poli 2017). The process applied in this study is detailed in Supplementary Information S-1.

An ambient vibration technique using arrays of stations was also carried out to get the 1D Vs profile below the array. A recent guideline along with the description of the acquisition and processing can be found in Foti et al. (2018). This technique offers the advantage of not requiring energetic seismic sources to investigate structures at depth. Two concentric circular arrays with diameters of 20 m and 100 m were deployed to cover a wide range of frequencies (see location in Fig. 1). Each network was composed of 12 three-component velocimeters synchronized by the GPS time of their acquisition station. Ambient vibrations were recorded during 1 h for each array with a sampling frequency of 100 Hz. Data were processed separately for the two arrays with the Rayleigh three-component beam forming technique (RTBF, Wathelet et al. (2018)). Experimental dispersion curves of the fundamental

and first higher propagation modes were separated. For each mode, the mean and the standard deviation were calculated for all available frequencies. The curves from the two arrays were jointly inverted with the neighborhood algorithm (Wathelet 2008), assuming a 3-layer parameterization based on the seismic stratification of the Avignonet landslide (Jongmans et al. 2009; Renalier et al. 2010). Misfit values between experimental and forward-modeled dispersion curves were calculated for both modes according to Eq. (1):

$$misfit = \sqrt{\frac{1}{n}\sum_{i=1}^{n}\frac{(\log(x_{di})-\log(x_{ci}))^2}{\log(\sigma_i)2}} \quad (1)$$

with $x_{di}$the ith experimental velocity, x_{ci} the ith modeled velocity, σ_i the ith standard deviation, and n the total number of experimental points considered across all modes.

Optical satellite images

Thirty-three satellite images from Sentinel-2 acquired between December 2015 and February 2019 were correlated in order to quantify displacement fields through time. This technique has been successfully applied on landslides (Delacourt et al. 2004; Debella-Gilo and Kääb 2012; Stumpf et al. 2014, 2017; Lacroix et al. 2015) and is well adapted to measure displacements larger than a fifth of a pixel size even in vegetated areas (Delacourt et al. 2004; Lazecký et al. 2015). The free Sentinel-2 optical images have a short revisit time (5 days at the equator) and offer the possibility to detect transient movements of landslides with a 1–2 m uncertainty (Lacroix et al. 2018, 2020; Mulas et al. 2020), such as those that affected the Harmalière slope between 2016 and 2018. Lacroix et al. (2018) performed a correlation analysis of Sentinel-2 images over 9 months during the major reactivation of June 2016 to quantify the transient acceleration of the landslide. In this study, the period of survey has been extended until 2019 over an area of 5 × 6 km^2 to detect possible subsequent events. Similarly to Lacroix et al. (2018), horizontal displacement fields between two images were calculated using the sub-pixel correlation algorithm implemented in Cosi-Corr (Leprince et al. 2007). The correlation was processed in the spatial domain using a square window of 24 pixels and a search radius of 500 m for all couples of images. Then, each correlation map was filtered with the method described by Lacroix et al. (2018), consisting in masking the points in each correlation pair with low quality (low CC, where the threshold of CC is adapted to each couple), or not in the slope direction. Also the methodology used by Lacroix et al. (2018) was adapted in two different ways to provide more robust results:

- First, all possible images were correlated together, and the system of redundant information was inverted to extract the displacement field at each date, following the methodology described in Bontemps et al. (2018). This time series algorithm was applied to the filtered correlations of the 14 images between September 2, 2016, and July 7, 2018, where enhanced filtering of displacement fields is required due to the season of their occurrence (rapid changes in surface conditions, snow, and cloud cover, fog, etc.).
- Then, the green (B3), blue (B2), and red (B4) bands of Sentinel-2 with 10 m resolution were processed. Finally, the three bands were combined by masking any displacement already filtered in one of the three bands. This process leads to uncertainty of the displacement varying between 1.2 and 2.4 m as calculated by the standard deviation of the EW and NS displacement fields over a stable area (of about 1 × 10^6 m^2).

LiDAR

The evolution of the landslide surface morphology was monitored using three sets of airborne LiDAR data collected on March 30, 2009, July 27, 2016, and November 26, 2019. The data in 2009 (resp. 2016–2019) were acquired using a Riegl laser scanner mounted on a helicopter flying at about 300 m (resp. about 600 m) above the ground, with an average density of 3 points m^{-2} (resp. 10 points m^{-2}) after classification. The altimetric and planimetric accuracies in 2009 and 2016–2019 were of 14 cm and 10 cm and of 25 cm and 10 cm, respectively. In order to retrieve a digital elevation model (DEM), the point clouds were filtered and interpolated on a raster grid of 2 × 2m^2 (2009) with the software SCOP++® (photo.geo.tuwien.ac.at/photo/software/scop/) and 1 × 1m^2 (2016-2019) with the software TerraSolid (www.terrasolid.com). To monitor changes in volume, the difference in elevation between two acquisitions was calculated using the QGIS software (www.qgis.org).

The two hillshaded LiDAR DEMs of 2016 and 2019 were also correlated using the sub-pixel correlation algorithm implemented in Cosi-Corr (Leprince et al. 2007) to obtain a horizontal velocity field between these dates. The hillshade operator was applied with a sun elevation of 45° and an azimuth of 315°. The azimuth of the light source corresponds to the direction of the landslide (NNW-SSE). The correlation was performed in the frequency domain using a window size of 128 pixels (1 m resolution), and then the same filtering processes as for optical images were applied. The process was not possible with the 2009 DEM because of large differences with other DEMs resulting from strong morphological changes during the reactivation of June 2016. This process leads to uncertainty of the displacement of about 1.3m as calculated by the standard deviation of the EW and NS displacement fields over a stable area (of about 1 × 10^5 m^2).

GNSS monitoring

Three permanent Geomon "low-cost" GNSS receiver units (www.infrasurvey.ch) have been installed about 10 m behind the headscarp since October 2017 (G2 to G4), and 5 others have been deployed along the landslide and in the stable zone since May 2018 (G1 and G5 to G8; see locations in Fig. 1). GNSS stations are compact (size of around 0.2 x 0.1 x 0.05 m^3) and connected to a base station using a radio protocol. The Geomon system receives GPS and GLONASS signals with the L1-band. The 3 stations at the rear of the headscarp are powered with 100 W solar panels and operate in a semi-permanent mode, acquiring 1-h-long records every 2 h. The 5 stations in the landslide are equipped with smaller 20 W solar panels, allowing for one 1-h session per day. The GNSS data were processed using the RTK-Lib software (Takasu et al. 2007). Positions are computed relatively to a reference station (AVR) located 2 km away and operated by the OMIV observatory (RESIF/OMIV, 2006). Results provided displacements with an

uncertainty of 1.5 cm horizontally and 2.4 cm vertically, as calculated by the standard deviation of the measurements of the G1 GNSS installed on a stable area. The location of G7 and G8 (Fig. 1) on the eastern side of the active earthflow (bottom part) area is motivated by the low vegetation in this area, in contrast to the central area of the bottom part of the landslide. Finally, it should be noted that stations G2 to G4 have been placed on the top of a 3-m-high tripod, resulting in a higher amplitude of displacements, especially rotation. Illustrations of the stations are provided in Supplementary Information S-2.

Results

Headscarp retrogression

Figure 3 a displays 6 aerial photos shot from 1948 to 2016, and Fig. 3 b shows the longitudinal topographic profiles in 1950 (extracted from IGN topographic map) and 2019 (from LiDAR DEM) with the evolution of the position of the headscarp between these two dates. Between 1948 and 2019, the headscarp has retrogressed by more than 700 m (Fig. 3a) with a major landslide that occurred in March 1981 (retrogression of 500 m) following by several reactivation phases (Moulin and Robert 2004; Bièvre et al. 2011, Table 1). In 70 years, the morphology of the slope has been considerably modified by the landslide, with a general smoothing and a vertical erosion of more than 50 m in the upper part, associated to a deposit of up to 80 m in the lower part (Fig. 3b).

Table 1 shows the retrogression areas for the periods highlighted in Fig. 3. Three characteristic sizes of events stand out: the main event in March 1981 (28 ha), two major events in 1988 and 2016 (around 2 ha each), and several minor events (< 1 ha).

Seismic activity

The seismic template-matching processing provides a catalog containing 6901 and 8223 landquakes at AVM and HAR2, respectively. This difference is due to the proximity of the sensors to the source and the slight different periods of acquisition. This continuous monitoring of landquakes allows the identification of four periods of intense activity: June 2016, November 2016, January 2017, and January 2018 (Fig. 4). The first active period started on June 25, 2016, and corresponds to a major reactivation of the Harmalière landslide. The number of daily events increased until June 28, 2016, and then decayed to the background level on July 7, 2016. Then, several peaks of seismic activity occurred in November 2016 (up to around 100 landquakes per day) and are concomitant with small ruptures at the headscarp (Fiolleau et al. 2020). The third major active period started on January 27, 2017, reached a peak of 2600 events per day at HAR2 on January 30, 2017. The GPS of a seismic sensor located on a large block prior to reactivation indicates that the blocks show significant displacement (10m) at the end of January 29, 2017 (during 13h30 from 13h30 UTM, Fig. 2). Finally, the seismic activity decreased back to the background level 2 weeks later. This third reactivation is associated with a rapid increase in average daily temperature from −3 °C to 6.8 °C between January 26 and January 27 (Fig. 4), causing important and rapid snow melt. A last period of significant seismic activity was detected between December 29, 2017, and January 7, 2018, corresponding to the last known reactivation event. For this period, HAR2 was out of order, and the event was only detected by AVM. As with the first event, precipitation did not exceed the seasonal average rate prior to this increase in seismic activity (Fig. 4).

Vs profile

The processing of the 1-h ambient vibrations records using the RTBF method (Wathelet et al. 2018) led to the Rayleigh wave dispersion maps (phase velocity as a function of the frequency) presented in Fig. 5a (small array) and 5b (large array). The layout of the array makes it possible to define the wavelength limits λ_{min} and λ_{max} (Fig. 5, Wathelet et al. 2008). Both figures highlight the fundamental and the first higher mode. The frequency ranges for these two modes are 3.1–18.3 Hz and 2.4–6.3 Hz, respectively. Taking into account the corresponding phase velocity values and the one-third wavelength rule for surface wave penetration (Tokimatsu 1997), a depth of investigation between about 2.5 m and 70 m can be expected.

Overall, the experimental and modeled values are in very good agreement (Fig. 5c). The corresponding 1D vs models are presented in Fig. 5d and show 3 layers with sharp velocity contrasts (vs values of about 150 m/s, 250 m/s, and 600 m/s) at 5–7 m and 30–35 m depth. These results are in agreement with the vs values and slip surface depths found in previous studies on the nearby Avignonet landslide (Jongmans et al. 2009; Renalier et al. 2010; Bièvre et al. 2012).

Landslide displacement

Figure 6 a to d show the displacement fields computed from four image pairs bounding the 2016 event. In June 2016, as shown by Lacroix et al. 2018, a succession of two major displacement phases can be observed: (1) the initiation of the reactivation at the headscarp, with a maximum displacement of about 5 ± 1.2 m between June 24 and 27 (Fig. 6a); (2) the largest movements took place between June 27 and July 7, with displacements of up to about 100 ± 1.3 m (Fig. 6b). Subsequently, from July 7 to August 3, a displacement of up to 62 ± 1.5 m occurred at the bottom of the landslide (Fig. 6c and d). Figure 6e shows the displacement field recovered during the processing of the 14 satellite images delineating the January 2017 reactivation. It was found that this event affected exclusively the upper part of the landslide, with displacements of up to 16 ± 2.4 m. The 2016–2019 DEM correlation provides a displacement field (Fig. 6f) that encompass the end of the 2016 reactivation, as well as the January 2017 and January 2018 reactivations (labelled A, B, and C, respectively). The displacements detected at the bottom of the landslide (from 20 ± 1.3 to 40 ± 1.3 m, Fig. 6f) are in agreement with the Sentinel-2 measurements (Fig. 6d) and show that the 2016 event ended in this area after August 3, 2016. The reactivation of January 2017 is clearly visible in the DEM correlation, with higher displacements (20 ± 1.3 to 30 ± 1.3 m) in the landslide upper part than those estimated with Sentinel-2 (Fig. 6e, 16 ± 0.3 m) but measured over a much longer time period (40 months versus 2 months). Finally, the 2018 reactivation, which was not detected by Sentinel-2 images correlation probably because of the small surface involved (1700 m^2), is just detectable on the DEM correlation with displacements up to 20 ± 1.3 m (Fig. 6f).

Continuous displacements measured at the 8 GNSS stations (G1 to G8) between April 2018 and April 2020 (i.e., after the last observed major reactivation of January 2018) are presented in

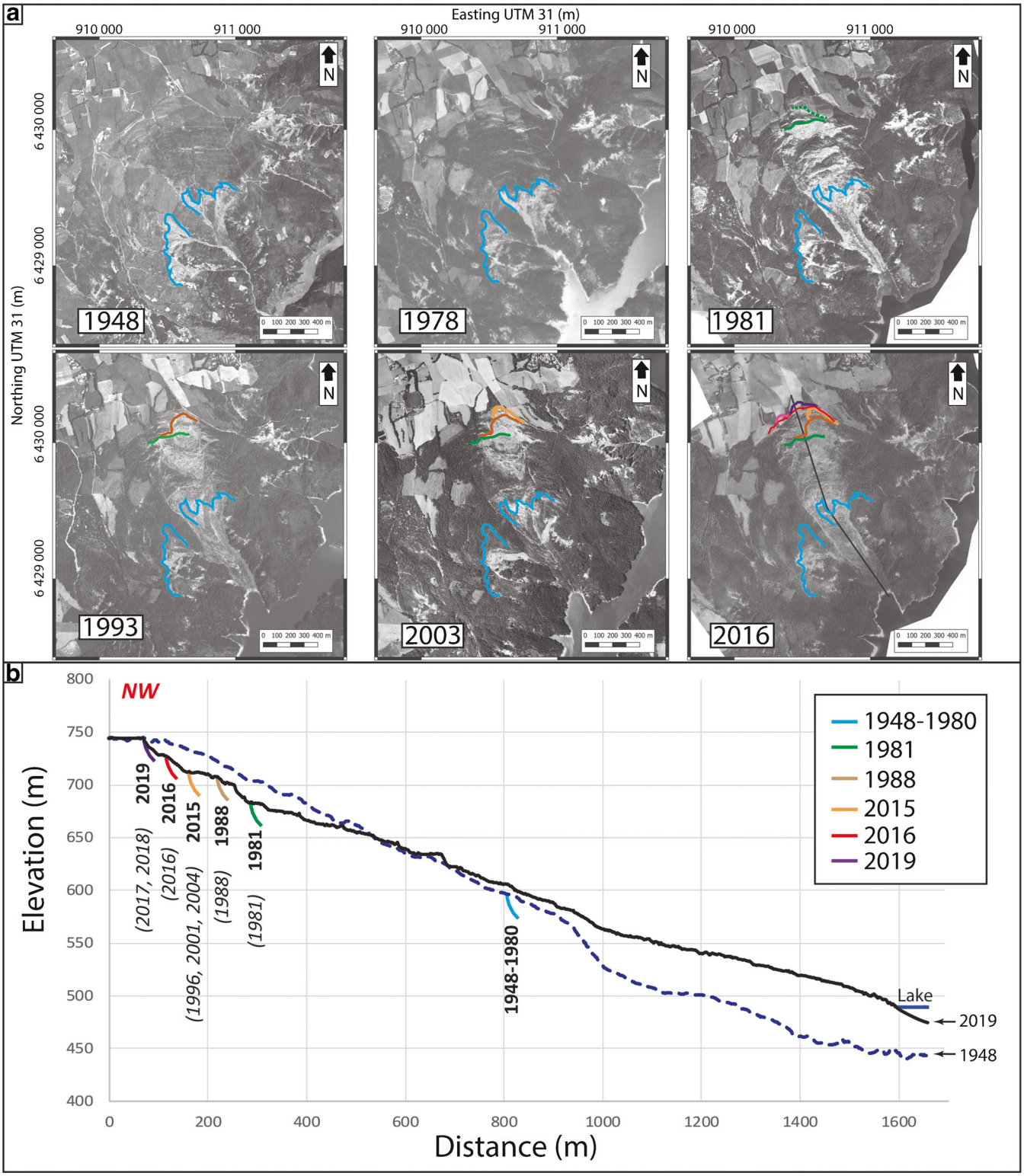

Fig. 3 Evolution and activity of the Harmalière landslide from 1948 to 2019. **a** Diachronic aerial photographs showing the successive locations of the main headscarp after the reactivation events of 1981, 1988, 1996, 2001, 2004, 2016, and 2017–2018 (colored lines, same color code as in Fig 3b). **b** NNW-SSE cross section of the landslide (location of the cross section in Fig. 1a, 2016; black line) showing the topographic profiles in 1950 (dashed line) and 2019 (plain line), along with the headscarp positions at given dates (bold font). The major reactivation events contributing to the retrogression are indicated in italic

Table 1 Retrogression area deduced from aerial photos and related events

Period	Retrogression area (ha)	Major events
1948–1980	0	None
1981	28	March 7, 1981
1982–1988	2.2	January 28–29, 1988
1989–2015	1	January 1996, 2001, 2004
2016	2.5	June–July 2016
2017–2019	0.9	January 2017 and 2018

Fig. 7. At the headscarp, displacement rates are zero for stations G2 and G3, and about 5 cm/year towards SSE for G4. In the upper mid-part of the landslide, stations G5 and G6 show continuous (Fig. 7b) displacement rates of 3 and 5 cm/year towards SE and S, respectively. At the toe of the slide, G7 and G8 show almost no displacement. The displacement rates measured by these stations (0.1 m/year maximum) are low compared to those obtained during reactivations (several m/day), but they indicate continuous landslide activity. They also suggest that the deformation mainly takes place in the upper-western and middle part of the landslide for the monitored period.

G5 (Fig. 7b), as G4, shows seasonal variations of their velocity with an amplitude of 3 cm/year and 8 cm/year, respectively. The two stations were positioned on a soft clayey material at 1 m and 3 m height respectively. The difference in elevation between the two stations results in the difference in amplitude variation (three times higher). The swelling and shrinking of the clay is probably the cause of this behavior.

Mass transfers

The overall mass depleted/accumulated over the 70 years of monitoring was assessed. From top to bottom of the landslide, this volume was estimated at about 6 $\times 10^6$ m^3 (difference between the DTM generated from the IGN topographic map of 1950 and the LiDAR DEM of 2019).

Figure 8a and b show the differences in elevation computed for the periods 2009–2016 and 2016–2019, respectively, and Fig. 8c shows NW-SE profiles of the differences in elevation for the 2 computed differences. Between 2009 and 2016, an erosion of up to 15–20 m (in red) at the two large upper scarps and lower material losses (5 to 8 m) along two lower scarps is observed. At the time of the second LiDAR acquisition (July 27, 2016), the lower part of the landslide was covered by a continuous deposit over a length of 800 m and with a maximum thickness of 16 m. A smaller deposit (up to 3 m thick) is also visible in the middle of the slope (Fig. 8a and c, between 250 and 400 m). Volume calculations provide similar estimates of about 1 $\times$ 10^6 m^3 for the mass depleted and accumulated.

Figure 8b shows differences in elevation computed for the periods 2016–2019. A NW-SE profile is shown in Fig. 8c (orange). A total depleted volume of about 2.5 $\times$ 10^5 m^3 was estimated, for an accumulation of about 2 $\times$ 10^5 m^3, with an estimated error of ± 0.5 $\times$ 10^5 m^3. At the toe of the landslide, a depletion of about 132 560 m^3 and an accumulation of about 80 000 m^3 was estimated, with an estimated error of ± 20 x 10^3 m^3. In the upper part, most of the depletion and accumulation took place along a 200-m-wide and 400-m-long strip. Most of the displaced mass resulted from headscarp retrogression, with maximum depletion and accumulation thicknesses of 12 m and 5 m, respectively (Fig. 8c).

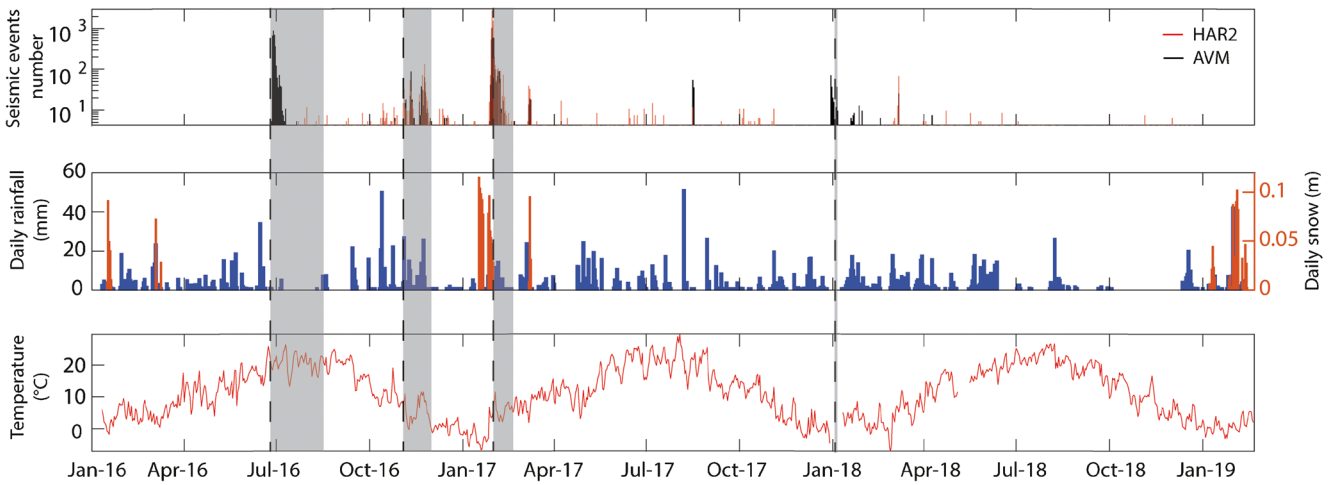

Fig. 4 Seismic activity and environmental parameters recorded on the Harmalière landslide between January 1, 2016, and February 20, 2019. **a** Daily landquakes detected at stations HAR2 (red) and AVM (black). **b** Daily rainfall (blue) and snow (red). **c** Daily temperature. Gray zones highlight the four reactivations that began on June 25,2016, November 3, 2016, January 28, 2017, and January 4, 2018

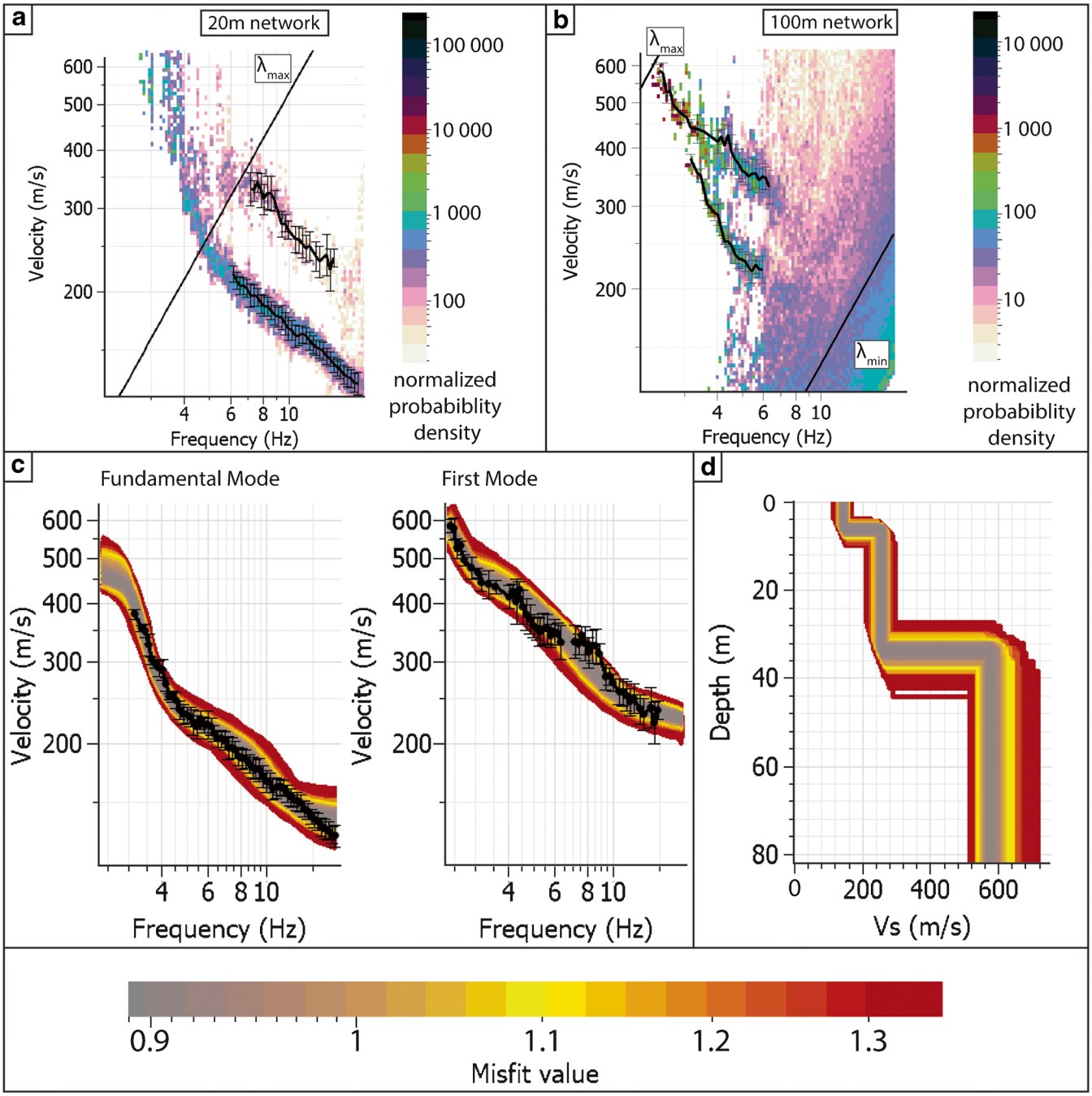

Fig. 5 Seismic noise analysis using the two arrays. **a** Dispersion histogram of the 20 m array and picked curves with error bars (black). **b** Dispersion histogram of the 100 m array and picked curves with error bars (black). **c** Rayleigh wave dispersion curves (black dots with error bars) picked for the fundamental mode (left) and the first higher mode (right) from the dispersion map. **d** Inverted vertical Vs profiles using the neighborhood algorithm (Wathelet 2008). Corresponding misfit values are indicated by colors on model results (Fig. 5d) and dispersion curves (Fig. 5c)

Interpretation

Structure of the landslide

An interpretative cross section of the Harmalière landslide was built (Fig. 9), using the following data: (1) the detailed topography of the slope provided by LiDAR imagery (2019) with the position of the scarps, from which the main slip surfaces are assumed to originate; (2) the depth of the two main slip surfaces indicated by the Vs profile (Fig. 5d); and (3) the bedrock geometry provided by the analysis of the seismic noise (Bièvre et al. 2011), geological observations, and the 1950 topography, assuming that the bedrock outcropped at the toe of the slide. In this cross section, the upper part of the landslide is characterized by a slope of around 11° and the presence of scarps with a rupture mechanism typical of a clay compound slide. The lower part exhibits a gentler and smoother slope (8°) and shows a flow-like morphology characteristic of an

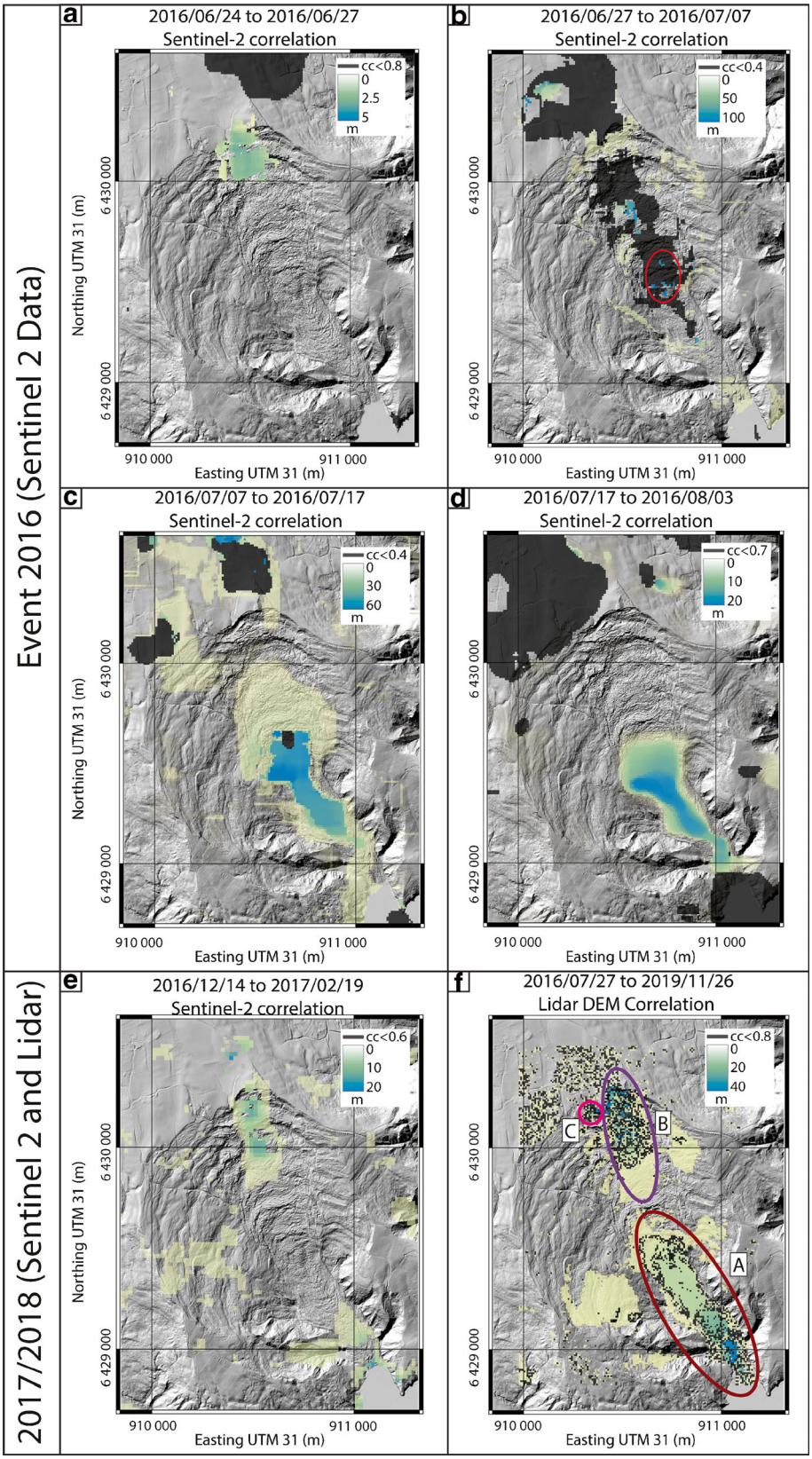

Fig. 6 Horizontal displacement fields calculated from Sentinel-2 images correlations for the **a** 2016/06/24–2016/06/27 period; **b** 2016/06/27–2016/07/07 period, red ellipse highlighted large displacement; **c** 2016/07/07–2016/07/17 period; **d** 2016/07/17–2017/08/03 period; and **e** 2016/12/14–2017/02/19 period. **f** Horizontal displacement field calculated from the Lidar DEMs (2016 and 2019) correlation for the 2016/07/27–2019/11/26 period. A: end of the 2016 event. B and C: location of the 2017 and 2018 reactivations, respectively. Black zones highlight low values of correlation coefficient (CC)

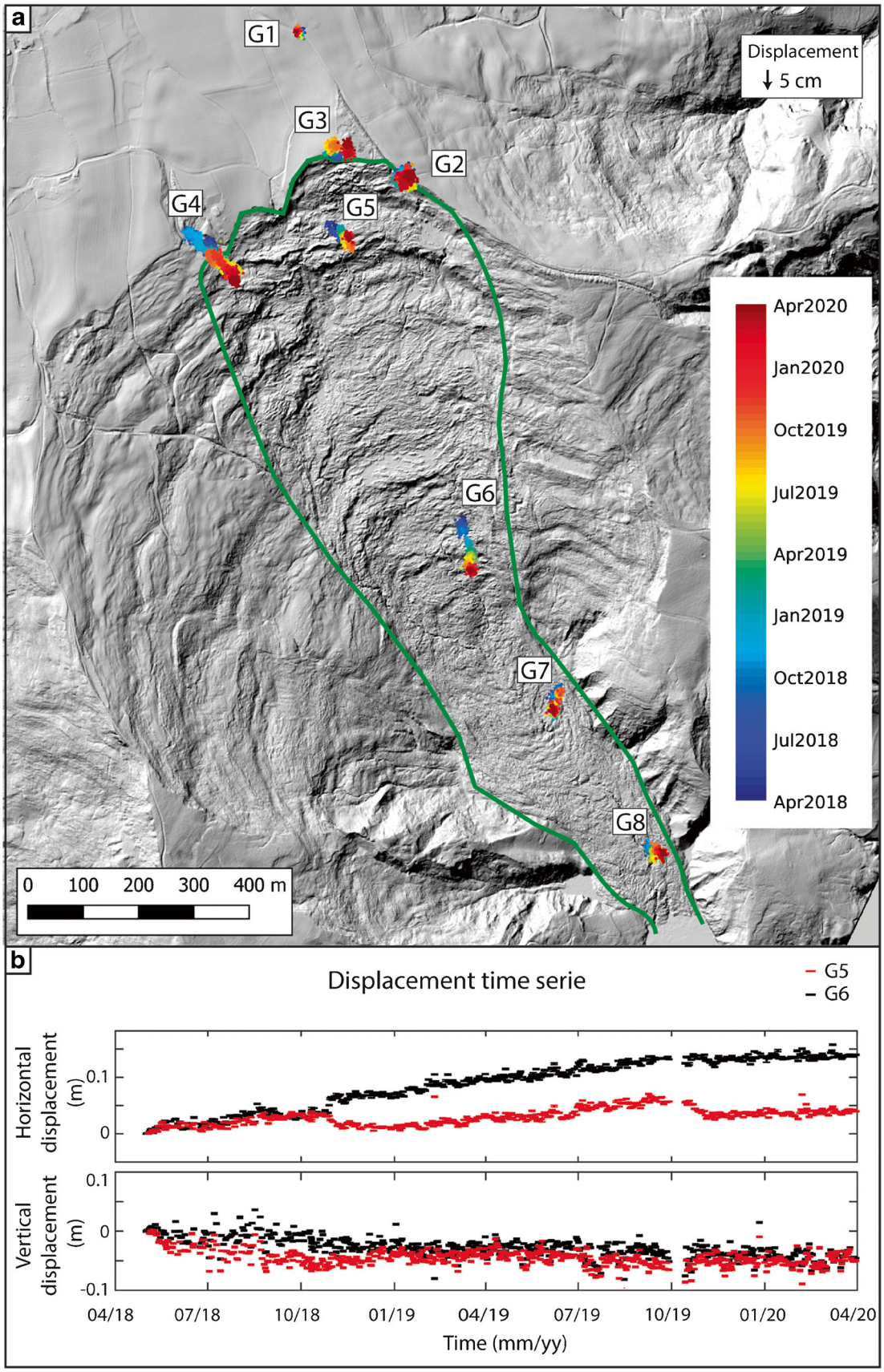

Fig. 7 **a** Horizontal displacement of the 8 GNSS Geomon sensors from April 2018 to April 2020 (scale represented by the arrow, multiplication factor of 173) **b** Displacement time series measured along the horizontal and vertical components of the Geomon stations G5 (red) and G6 (black)

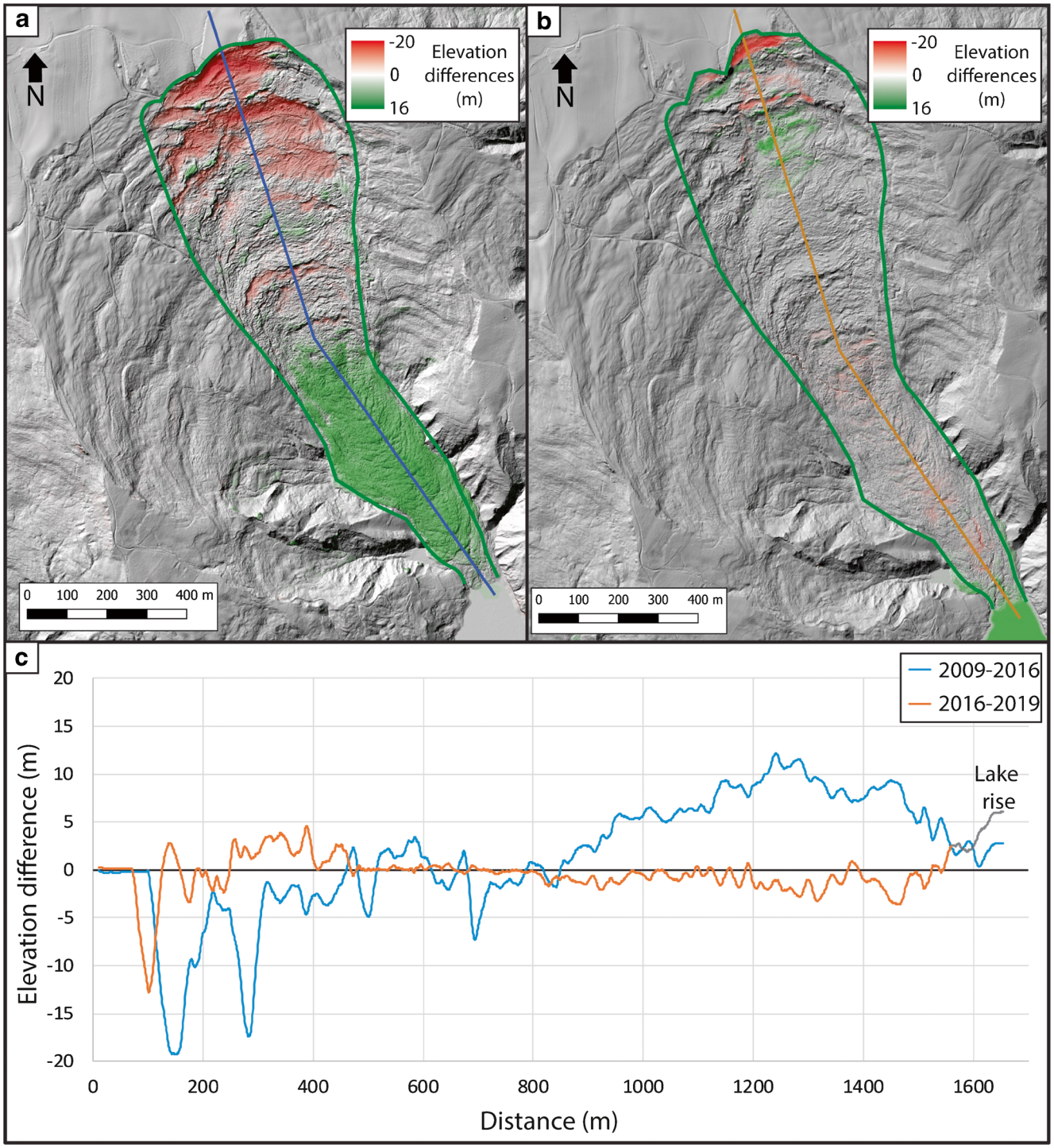

Fig. 8 Elevation differences computed between the LiDAR DEMs of **a** March 30, 2009, and July 27, 2016 and **b** July 27, 2016, and November 26, 2019. **c** NW-SE sections showing the elevation differences along the line drawn in Fig. 6a and b

earthflow. A transition zone between these two mechanisms can be identified between abscissa 450 and 1000 m along the section (Fig. 9). This transition zone is characterized by a bulge presumably induced by the presence of the bedrock uplift at this location. As shown in the cross section (Fig. 9), the two slip surfaces are connected to explain both the local deformation and the long-distance mass transfer. At the landslide toe, the earthflow behavior is associated with the presence of numerous accumulation lobes, presumably indicative of secondary daylighting slip surfaces. The volume of the whole Harmalière landslide was calculated on the basis of this section, extending the depth of the deeper slip surface laterally (Jaboyedoff et al. 2020). An estimated landslide volume of about 45×10^6 m^3 is obtained, which is significantly larger than the previous assessment of 25×10^6 m^3 made by Carrière et al. (2018).

Reactivation types

The landslide history over the last 70 years highlighted a significant headscarp retreat of about 700 m, characterized by sudden strong retrogressive events such as those of March 1981 (28 ha), January 1988 (2.1 ha), and June 2016 (2.5 ha). The increased amount of data since 2009 (Sentinel-2 images, LiDAR acquisitions, seismic data, GNSS) makes it possible to overcome this lack of information and to interpret the various mechanisms of the reactivation events.

Calculating the differences between the three LiDAR DEMs of 2009, 2016, and 2019 allowed to estimate and locate the depleted/accumulated volumes during the reactivation events of June 2016 and January 2017/January 2018. As no significant changes in morphology were observed in aerial photos between March 2009 and June 2016, the differences in elevation between these dates (Fig. 8a) are assumed to be entirely due to the event of June–July 2016. The second LiDAR acquisition, which took place on July 27, 2016, shows that, during this reactivation phase, most of the 1×10^6 m^3 volume was transferred from the upper to the lower part within a maximum of 1 month. This mass transfer, which was measured thanks to Sentinel-2 correlation, occurred during the most active phase (between July 7 and 17, 2016) with a displacement rate of up to 10 m/day. Differences between the 2019 and 2016 DEMs include the cumulative effect of the events of January 2017, January 2018, and the end of the 2016 event for a total depleted volume of about 2.5×10^5 m^3 and an accumulated volume of about 2×10^5 m^3. However, the areas concerned by these three events were identified using the displacement fields recovered from the correlation of the Sentinel-2 images. The volume for each area was then calculated by the difference of DEM (2019–2016). The mass movement induced by the end of the 2016 event was observed at the toe of the landslide with a depletion of about $132{,}560 \pm 2 \times 10^4$ m^3 and an accumulation of about $80{,}000 \pm 2 \times 10^4$ m^3. The difference in volume may have flown into the lake or resulted from the change in lake level, which was 6 m higher in 2019 than in 2016. In the upper part, the depletion induced by the event of January 2017 amounted to $112{,}340 \pm 3 \times 10^4$ m^3, for an accumulation of about $113{,}800 \pm 3 \times 10^4$ m^3, while the small reactivation in 2018 depleted only $7067 \pm 1.4 \times 10^3$ m^3 for an accumulation of about $8110 \pm 1.4 \times 10^3$ m^3.

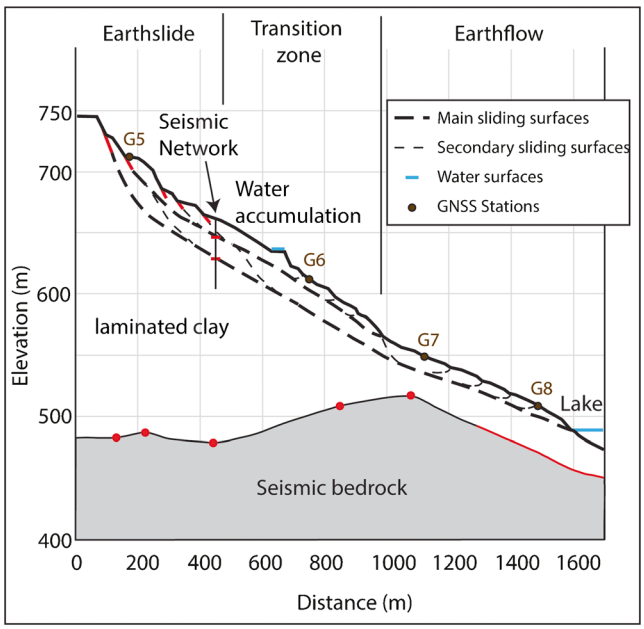

Fig. 9 Interpretative cross section of the Harmalière landslide from the topography extracted from the LiDAR DEM acquired in November 2019. Red dots: bedrock roof from H/V measurements refined from Bièvre et al. (2011) results. Red part of the bedrock corresponds to the 1950 topography. Red bars: constraints on the scarps and shear surface deduced from the seismic network

Considering the volume and surface area involved, the Harmalière landslide showed two types of reactivation. Major events such as those of 1981 and 2016 reactivated the entire landslide involving a large volume of material ($> 10^6$ m^3). On the other hand, smaller events, such as those of 2017 and 2018 ($< 1.2 \times 10^5$ m^3), affected only the upper part of the landslide, with the transition zone showing no displacement during these events. In order to better understand the difference between these two types of events, a focus is made on the reactivation mechanism of the 2016 and 2017 events.

Reactivation mechanisms

The two reactivation events of 2016 and 2017 both displayed intense seismic activity and large displacements. Despite these similarities, these two events also show prominent differences regarding (i) the size and distribution of the mass transfer and (ii) the season of occurrence (dry and wet), providing an opportunity to study the mass transfer mechanism along the landslide with more details. Geodetic, kinematic, and seismic activity data have all been combined to obtain a comprehensive view of the two events. The smaller January 2017 event is analyzed first.

January 2017 event

Figure 10a shows the displacement field associated to this event, as well as the depleted (red) and accumulated (green) volumes. An interpretative NS section is displayed in Fig. 10b with the 2016 and 2019 topographies. The mechanism of this reactivation appears to be a compound slide initiated at the headscarp along a listric shallow slip surface, leading to a back-tilting of the upper bench. This slip surface is divided into several active branches that generate convex accumulation lobes (Fig. 10a and b). Mass transfer takes place over these multiple branches down to a distance of 350 m from the headscarp, as shown by optical image correlation (Fig. 6e). This large distance, and the formation of multiple lobes, suggests that the two main slip surfaces of the landslide (bold dotted lines, Fig. 10b) have been reactivated. The lack of material accumulated in the central part, which is a consequence of the previous 2016 event (see below), probably prevents the propagation of the mass transfer over the entire landslide area.

The seismic activity curve (Fig. 10c) shows a sudden increase, a peak, and a slow decay, corresponding to the initiation (Fig. 2b), the main rupture and the final accommodation of the reactivation. Combined examination of the microseismicity and meteorological conditions shows that the initial failure occurred during a phase of warming (−3 to 7 °C in 1 day) and snow melt accompanied by a gradual increase in the number of landquakes. The seismic activity was maximum at the time of the reactivation (Fig. 2b) and then decreased over a period of about 15 days (relaxation phase), showing a significant activity during 10 days. This time period provides an order of magnitude of the mass transfer time. Contrary to

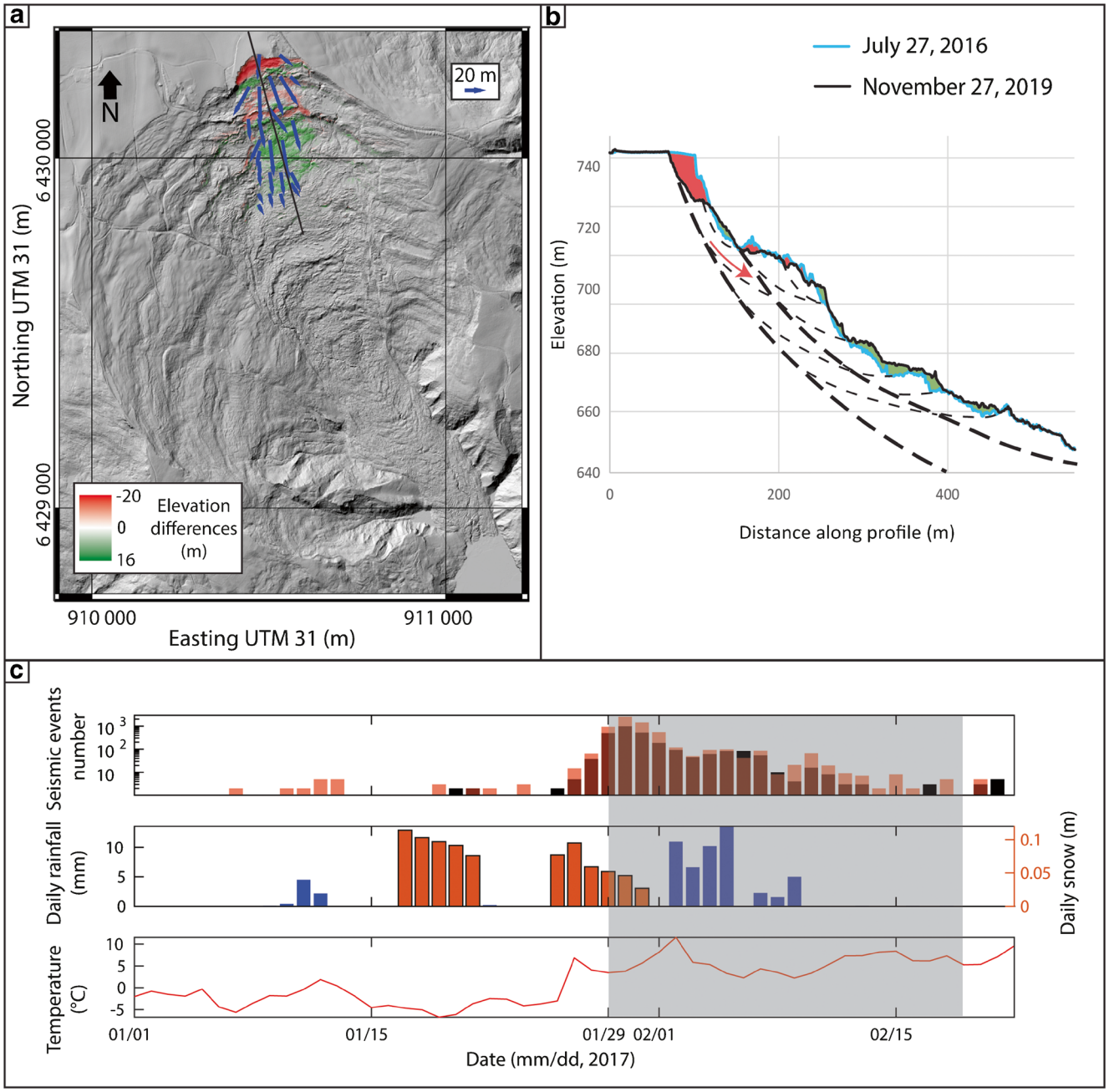

Fig. 10 Interpretation of the mass transfer for the January 2017 event. **a** Elevation differences and displacement field (blue arrows) shown on the 2019 DEM. The black line indicates the position of the cross section in **b**. **b** Interpreted cross section. Areas of erosion and deposition are highlighted in red and green, respectively. The two main deep sliding surfaces are indicated by bold dashed lines. Secondary slip surfaces are indicated by thin dashed lines. **c** Seismic events number (from AVM in black and HAR2 in red), daily precipitations (blue), daily snow (orange), and temperature variations over the period 01/01/2017 to 22/02/2017. The gray zone highlights the duration of the reactivation event extracted from the seismic activity

previous studies (Yamada et al. 2016; Poli 2017), no repeating events, with highly similar waveforms, quasi periodic occurrence times, and progressive changes in amplitude and recurrence times, were observed. In contrast, seismic events are clustered in time and display power-law distribution of peak amplitude and inter-event times. This suggests that landquakes are not associated with the repeated rupture of asperities during the progressive nucleation of the main rupture, as proposed by Yamada et al. (2016) and Poli (2017). Landquakes at Harmalière landslide may rather be produced by the propagation of new slip surfaces.

June 2016 event

The June 2016 event is one of the three major reactivation events that occurred in the Harmalière landslide since it was activated (Table 1). The amount of precipitation observed prior to this event was not particularly high (< 10 mm after June 16, 2016). The five

Sentinel-2 images available over the 40 days of the reactivation (between June 24 and August 8, 2016) were used to interpret the different stages of the reactivation. The depleted/accumulated volumes for each stage were estimated from the displacement fields and the total depleted/accumulated volumes calculated from the differences between the 2009 and 2016 DEMs. In the upper part of the landslide, the difference in volume between DEMs is divided between the two periods June 24–27 (Fig. 11a) and June 27–July 7 (Fig. 11b) showing horizontal displacements. From the transition zone to the landslide toe, the depleted/accumulated volumes are distributed between the three periods June 27–July 7, July 7–27, and July 27–August 3 (Fig. 11 b, c, and d, respectively). Thus, an estimation of the depleted/accumulated volumes for each period was made according to the displacement rate of the period (a low displacement rate gives a low volume). Figure 11a to d shows, at these 4 different periods, the displacement field and the interpretation of the mass transfers with the depleted and accumulated volumes in red and green, respectively. The corresponding interpretation is shown on longitudinal sections in Fig. 12, with the last 2 periods (July 7 to July 17, 2016, and July 17 to August 3, 2016) grouped in Fig. 12c.

Regarding the seismic activity, the initiation phase occurred between the 25 and 27 of June. During this initial phase, the main movement consists of relatively superficial and low amplitude (5 m in horizontal displacement) sliding, affecting the two upper scarps (Figs. 6a, 11a) and creating an accumulation at their foot where slip surfaces daylight (between 200 and 350 m, Fig. 12a). This initial destabilization mechanism appears to be relatively similar to the 2017 reactivation with mass transfer occurring up to 350 m from the headscarp. The abrupt increase in seismic activity (Fig. 11e) seems to indicate that the onset of larger movements (metric) occurs on June 25. On June 27, a large deep slide with a horizontal surface displacement of 100 m detected by the Sentinel-2 images is triggered (Figs. 11b and 12b). Seismic activity peaks on June 28 and then decreases steadily (Fig. 11e). This second phase shows a displacement from the headscarp to the end of the transition zone, with a displaced volume of about 1×10^6 m^3. Multiple slip surfaces daylighting in the slope created a series of lobes in the transition zone (Fig. 12b, between 800 and 1000 m). The main mechanism during this phase is translational sliding along slip surfaces, which is assumed to generate the seismic activity.

After July 7, mass transfer exclusively took place from the transition zone to the landslide toe, with a first active phase (Fig. 11c) during which surface displacements are of the order of 60 m. This phase is associated with a decrease in seismic activity between July 7 and 13, which can be explained by (i) the onset of a flow-like mechanism with less friction and (ii) the larger distance between sensors and the active area. From July 13 to August 3 (Fig. 11d and e), a last phase is observed with smaller surface displacements of the order of 20 m and only weak and irregular seismic activity. The overall mass transfer from the transition zone to the lower part of the landslide between July 7 and August 3 is shown in cross section in Fig. 12c. The main mechanism during these two phases appears to be earthflow with a very large number of slip surfaces.

As previously indicated, the main mechanism in the transition zone is translational slide, although some scarps and lobes may also be due to very shallow sliding surfaces. This translational mechanism is confirmed by the presence of blocks that retain a similar morphology during movement and whose displacements are deduced from the correlations of the Sentinel-2 images (Fig. 7 and Fig. 11). These blocks are shown (*b1* and *b2*) in the profiles of Fig. 12. Block *b1* began its movement with a slight vertical displacement of a few meters (Fig. 12a) during the initiation phase. Then, during the main movement phase, blocks b1 and b2 slid along the shallower slip surface, probably dragged by the deeper slip surface as well, with a displacement of around 200 m for b1 and around 100 m for b2 (Fig. 12b). These interpretation shows that the displacements detected by Sentinel-2 (up to 100m) are smaller than the actual displacements. The difference in displacement between the two blocks implies the presence of a sliding surface generating lobes between the two blocks (Fig. 12b, at 500 m). Finally, during the last phases from July 7 to August 3, the two blocks moved a further 30 m and 100 m, respectively, remaining in the transition zone (Fig. 11c).

Transition zone influence

In terms of kinematics and rheology, the two events of 2016 and 2017 showed that motion in the upper part of the landslide is characterized by a rigid-like behavior, with sliding along uneven slip surfaces divided into several branches. Beyond the transition zone, the mechanism becomes flow-like, as shown by the development of a lobate morphology after the 2016 event. In this lower part of the landslide, the material undergoes solid-viscous transition with the generation of a mudflow, as was the case in the 1981 event, or of an earthflow, as in the June 2016 event, presumably depending on its water content. In contrast, for smaller reactivation events characterized by a tenfold smaller depleted volume in 2017/2018, the mass was only displaced to a maximum distance of 350 m. The mobilized volume was not sufficient to reach the transition zone, suggesting a threshold volume value for long-range mass transfer along the landslide. In addition, the 2016 event, which started similarly as the 2017 event, may have benefited from the cumulative accumulations of previous smaller events. The accumulation of material in this transition zone allowed a fast transfer speed (up to 10 m/day, during the most active phase; Fig. 6), which freed the space in front of the headscarp, and explains the constant maintenance of a cliff at the top of the slide in the most active zone. The mechanism of this zone is probably influenced by the bulging of the bedrock (Fig. 9), allowing the clay material to accumulate prior to earthflow. GNSS data acquired after the 2017 event over a period of 2 years indicate that the slope is subject to a permanent slow downward motion of up to 0.1 m/year.

These results show the key role of the transition zone in the mass transfer mechanism within the Harmalière landslide. The material accumulates there during small reactivations as in 2017, undergoing during its displacement a progressive degradation preparing it for a flow-like behavior. A major event, such as that of June 2016, reactivates the entire landslide and purges the transition zone, generating either an earthflow (June 2016) or a mudflow (March 1981), depending on whether the water supply is high or low.

Conclusions

A morphological and kinematic study of the Harmalière clayey landslide was conducted over a 70-year period. Results show that the headscarp has retrogressed by 700 m, with a mass depleted/

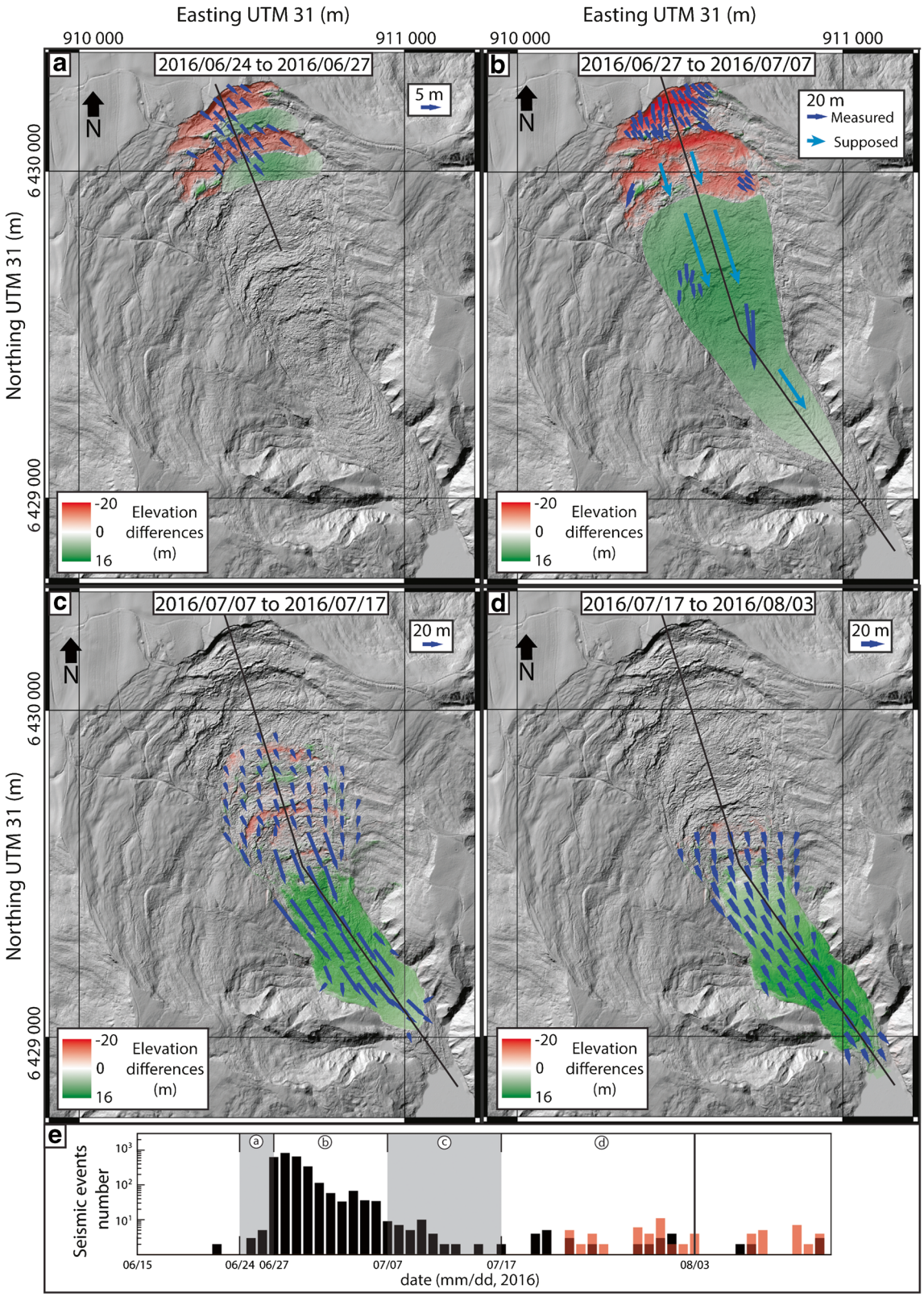

Fig. 11 Interpretation of the mass transfer during the 2016 reactivation event: height differences and field displacement (blue arrows) during the event. **a** June 24 to 27, **b** June 27 to July 07, **c** July 07 to 27, and **d** July 27 to August 3. The black line indicates the position of the cross sections shown in Fig. 12. **e** Number of landquakes detected during these 4 periods (**a** to **d**), with the events recorded at HAR2 in red (installed on July 22, 2016) and those at AVM in black

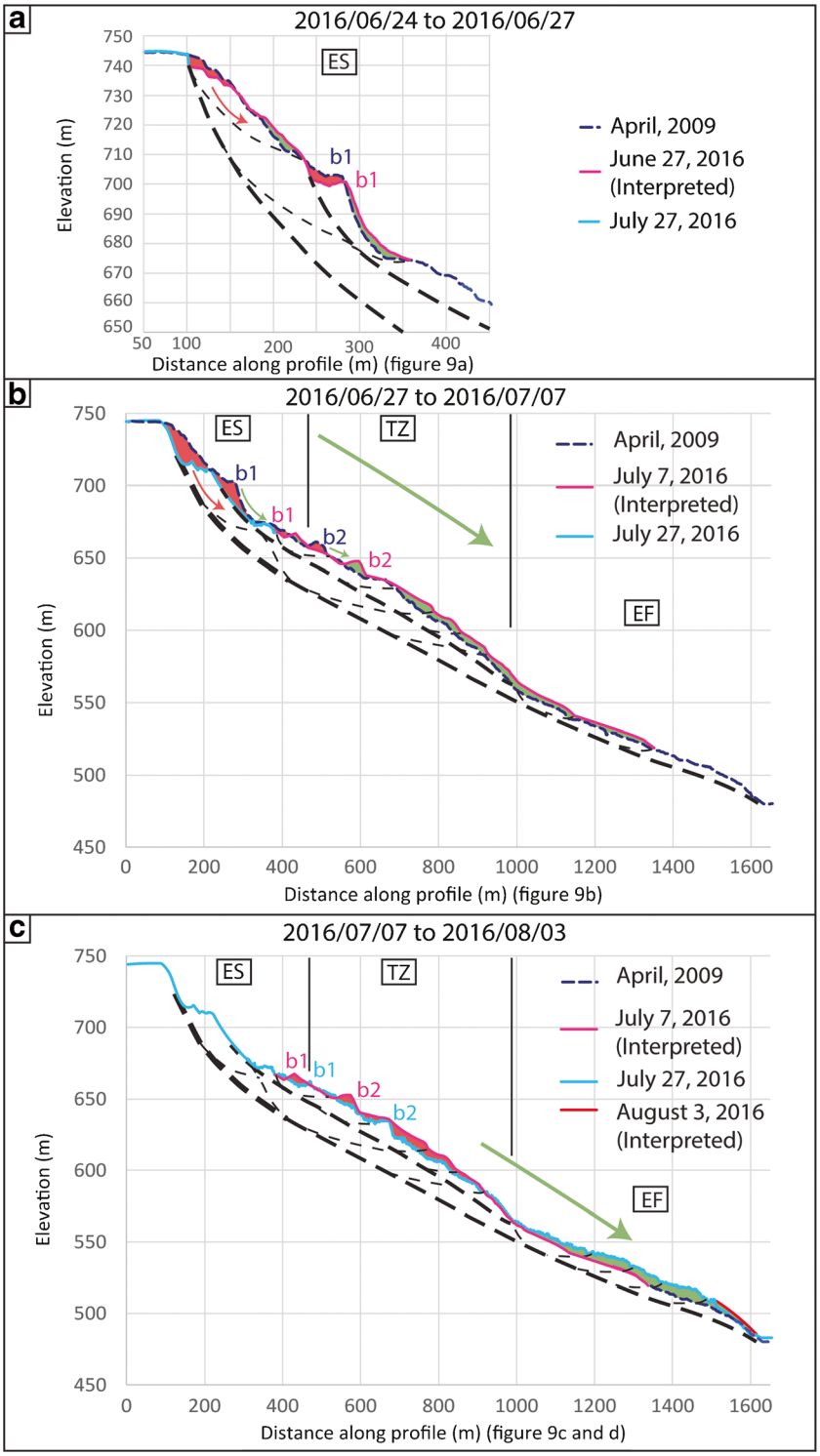

Fig. 12 Mass transfer interpretative cross sections for the 2016 reactivation event. **a** June 24 to June 27, **b** June 27 to July 07, and **c** July 07 to August 3. Zones of erosion and deposition are highlighted in red and green, respectively. The two main deep slip surfaces are indicated by bold dotted lines. The red and green arrows correspond to the rotational movements and mass transfer, respectively. ES, TZ, and EF correspond to the earthslide, transition, and earthflow zones, respectively

accumulated from the top to the bottom of the landslide of around 6×10^6 m^3. Over the last 40 years, the average retrogression rate of the landslide is on the order of 5 m/year. The sliding mechanism regularly affects the headscarp that remains constantly steep and unstable with a height of up to 30 m. During this 70-year period, three major events happened (1981, 1982–1988, 2016), of which two are documented (1981, 2016) and occurred in very different meteorological conditions. The main reactivation of March 1981 was

triggered after an episode of rain on a 0.4 m thick layer of snow. It affected an area of around 45 ha and caused the headscarp to suddenly regress by more than 500 m in 1 day. No data are available on the volume displaced. The June 2016 event, triggered in dry conditions, affected an area of 2.5 ha and contributed to the transfer of 1×10^6 m^3 to the base of the landslide. The detailed study of this last event established that the mass transfer was achieved in the course of 5 weeks, with a slide mechanism at the top and earthflow at the toe.

In terms of methodology, this study showed the complementarity between ground data (seismic, GNSS) and remote sensing (optical satellite images, airborne LiDAR) monitoring techniques. First, the correlation of Sentinel-2 images offers the possibility to obtain surface displacement fields with a temporal resolution of a few days to a few weeks (revisit time of 5 days for Sentinel-2) and a spatial resolution of the order of 1 m. Then, the three LiDAR acquisitions, carried out at intervals of several years, covered the entire landslide and provided accurate data on 3D displacements and depleted volumes over time periods containing one or two reactivation episodes. This technique provides a detailed topographic information with a spatial resolution of 0.1m and allowed to monitor the mass transfers that occurred during the reactivation. Complementary seismic surveys allowed to locate slip surfaces at depth along with the depth to the bedrock that controls the mass transfer. Seismic monitoring using template-matching filtering allows a real-time, remote, and automatic detection of reactivation phases. Additional sensors should be installed close to the landslide in order to locate the seismic sources. Finally, low-cost GNSS monitoring provides spatially punctual data with very high temporal resolution (0.5 pt/h to 1 pt/day in this work) that allows to track the 3D displacement between two reactivations. However, an event such as the sudden reactivation of 2016 could have interrupted the operation of the instruments installed on the ground, or even destroyed them. In the future, the implementation of low-cost GNSS sensors, the acquisition of cheaper and more flexible LiDAR data by unmanned aerial vehicles, and the free availability of higher spatial resolution satellite data (such as Pléiades) open up both scientific and operational prospects for improving the monitoring and understanding of such gravitational movements.

Supplementary Information The online version contains supplementary material available at https://doi.org/10.1007/s10346-021-01639-z.

Acknowledgements

Meteorological data were provided by OMIV (Multidisciplinary Observatory of Versant Instabilities; (www.ano-omiv.cnrs.fr). The authors thank two anonymous reviewers and the editor who greatly helped to enhance the quality of this paper.

Funding The authors acknowledge the financial support from the French VOR federative structure, the French national C2ROP project, the French National Research Agency in the framework of the Investissements d'Avenir program (ANR-15-IDEX-02, CDP-RISK), and the LabEx OSUG@2020 (ANR10 LABX56). This work was partly supported by the project SIMOTER 1 funded by the European Union under the ERDF – POIA program and by the French government under the FNADT – CIMA program.

References

Al Hayari M, Antoine P, Biguenet G, Monnet J, Mora H (1990) Détermination des caractéristiques mécaniques au cisaillement des argiles litées. Cas du glissement de la combe d'Harmalière. Rev Fr Géotech (50):71–77

Baum RL, Messerich J, Fleming RW (1998) Surface deformation as a guide to kinematics and three-dimensional shape of slow-moving, clay-rich landslides, Honolulu, Hawaii. Environ Eng Geosci 4:283–306. https://doi.org/10.2113/gseegeosci.iv.3.283

Bertello L, Berti M, Castellaro S, Squarzoni G (2018) Dynamics of an active earthflow inferred from surface wave monitoring. J Geophys Res Earth Surf 123:1811–1834. https://doi.org/10.1029/2017JF004233

Besson L (1996) Les risques naturels en montagne: traitement, prévention, surveillance. Artès-publialp

Bièvre G, Jongmans D, Winiarski T, Zumbo V (2012) Application of geophysical measurements for assessing the role of fissures in water infiltration within a clay landslide (Trièves area, French Alps). Hydrol Process 26:2128–2142. https://doi.org/10.1002/hyp.7986

Bièvre G, Kniess U, Jongmans D, Pathier E, Schwartz S, van Western C, Villemin T, Zumbo V (2011) Paleotopographic control of landslides in lacustrine deposits (Trièves plateau, French western Alps). Geomorphology 125:214–224. https://doi.org/10.1016/j.geomorph.2010.09.018

Bontemps N, Lacroix P, Doin M-P (2018) Inversion of deformation fields time-series from optical images, and application to the long term kinematics of slow-moving landslides in Peru. Remote Sens Environ 210:144–158. https://doi.org/10.1016/j.rse.2018.02.023

Carrière S, Bièvre G, Jongmans D, Chambon G, Bellot H, Lebourg T (2018) Measurement of geophysical parameters on clay samples at the solid–fluid transition. Near Surf Geophys 16:23–37. https://doi.org/10.3997/1873-0604.2017039

Carson MA (1977) On the retrogression of landslides in sensitive muddy sediments. Can Geotech J 14:582–602. https://doi.org/10.1139/t77-059

Coltorti M, Tognaccini S (2019) The gravitational landscape of Montespertoli (Valdelsa Basin, Tuscany, Italy): state of activity and characteristics of complex landslides. Geomorphology 340:129–142. https://doi.org/10.1016/j.geomorph.2019.04.030

Comegna L, Picarelli L, Urciuoli G (2007) The mechanics of mudslides as a cyclic undrained–drained process. Landslides 4:217–232. https://doi.org/10.1007/s10346-007-0083-2

Corominas J, Moya J, Ledesma A, Lloret A, Gili J (2005) Prediction of ground displacements and velocities from groundwater level changes at the Vallcebre landslide (Eastern Pyrenees, Spain). Landslides 2:83–96. https://doi.org/10.1007/s10346-005-0049-1

Cruden D, Varnes DJ (1996) Landslide types and processes. In: Turner A, Schuster R (eds) Landslides investigation and mitigation. National Academic Press, Washington, pp 36–75

Debella-Gilo M, Kääb A (2012) Measurement of Surface Displacement and Deformation of Mass Movements Using Least Squares Matching of Repeat High Resolution Satellite and Aerial Images. Remote Sens 4:43–67. https://doi.org/10.3390/rs4010043

Delacourt C, Allemand P, Casson B, Vadon H (2004) Velocity field of the "La Clapière" landslide measured by the correlation of aerial and QuickBird satellite images. Geophys Res Lett 31. https://doi.org/10.1029/2004GL020193

Demers D, Robitaille D, Locat P, Potvin J (2014) Inventory of large landslides in sensitive clay in the province of Québec, Canada: preliminary analysis. J.-S. L'Heureux et al (eds), Landslides in sensitive clays: from geosciences to risk management. Adv Nat Technol Hazards Res 36:77–89. https://doi.org/10.1007/978-94-007-7079-9

Fernandez P, Whitworth M (2016) A new technique for the detection of large scale landslides in glacio-lacustrine deposits using image correlation based upon aerial imagery: a case study from the French Alps. Int J Appl Earth Obs Geoinf 52:1–11. https://doi.org/10.1016/j.jag.2016.05.002

Fiolleau S, Jongmans D, Bièvre G, Chambon G, Baillet L, Vial B (2020) Seismic characterization of a clay-block rupture in Harmalière landslide, French Western Alps. Geophys J Int 221:1777–1788. https://doi.org/10.1093/gji/ggaa050

Foti S, Hollender F, Garofalo F et al (2018) Guidelines for the good practice of surface wave analysis: a product of the InterPACIFIC project. Bull Earthq Eng 16:2367–2420. https://doi.org/10.1007/s10518-017-0206-7

Gibbons SJ, Ringdal F (2006) The detection of low magnitude seismic events using array-based waveform correlation. Geophys J Int 165:149–166. https://doi.org/10.1111/j.1365-246X.2006.02865.x

Giordan D, Allasia P, Manconi A, Baldo M, Santangelo M, Cardinali M, Corazza A, Albanese V, Lollino G, Guzetti F (2013) Morphological and kinematic evolution of a large earthflow: the Montaguto landslide, southern Italy. Geomorphology 187:61–79. https://doi.org/10.1016/j.geomorph.2012.12.035

Giraud A, Antoine P, Van Asch TWJ, Nieuwenhuis JD (1991) Geotechnical problems caused by glaciolacustrine clays in the French Alps. Eng Geol 31:185–195. https://doi.org/10.1016/0013-7952(91)90005-6

Gregersen O (1981) The quick clay landslide in Rissa, Norway. Proceedings of the 10th International Conference on Soil Mechanics and Foundation Engineering, Stocholm, vol. 3, pp. 421–426

Gunn DA, Chambers JE, Hobbs PRN, Ford JR, Wilkinson PB, Jenkins GO, Merritt A (2013) Rapid observations to guide the design of systems for long-term monitoring of a complex landslide in the Upper Lias clays of North Yorkshire, UK. Q J Eng Geol Hydrogeol 46:323–336. https://doi.org/10.1144/qjegh2011-028

Helmstetter A, Garambois S (2010) Seismic monitoring of Séchilienne rockslide (French Alps): analysis of seismic signals and their correlation with rainfalls. J Geophys Res 115:F03016. https://doi.org/10.1029/2009JF001532

Helmstetter A, Moreau L, Nicolas B, Comon P, Gay M (2015) Intermediate-depth icequakes and harmonic tremor in an Alpine glacier (Glacier d'Argentière, France): evidence for hydraulic fracturing? J Geophys Res Earth Surf 120:402–416. https://doi.org/10.1002/2014JF003289

Hungr O, Leroueil S, Picarelli L (2014) The Varnes classification of landslide types, an update. Landslides 11:167–194. https://doi.org/10.1007/s10346-013-0436-y

Jaboyedoff M, Carrea D, Derron M-H, Oppikofer T, Penna IM, Rudaz B (2020) A review of methods used to estimate initial landslide failure surface depths and volumes. Eng Geol 267:105478. https://doi.org/10.1016/j.enggeo.2020.105478

Jaboyedoff M, Oppikofer T, Abellán A, Derron M-H, Loye A, Metzger R, Pedrazzini A (2012) Use of LIDAR in landslide investigations: a review. Nat Hazards 61:5–28. https://doi.org/10.1007/s11069-010-9634-2

Jongmans D, Bièvre G, Renalier F, Schwartz S, Beaurez N, Orengo Y (2009) Geophysical investigation of a large landslide in glaciolacustrine clays in the Trièves area (French Alps). Eng Geol 109:45–56. https://doi.org/10.1016/j.enggeo.2008.10.005

Kohv M, Talviste P, Hang T, Kalm V, Rosentau A (2009) Slope stability and landslides in proglacial varved clays of western Estonia. Geomorphology 106:315–323. https://doi.org/10.1016/j.geomorph.2008.11.013

L'Heureux JS (2012) A study of the retrogressive behaviour and mobility of Norwegian quick clay landslides. Proc. of the 11th Int. & 2nd North American Symp. on Landslides, Banff, Canada, 3–8 June 2012

Lacroix P, Araujo G, Hollingsworth J, Taipe E (2019) Self-entrainment motion of a slow-moving landslide inferred from landsat-8 time series. J Geophys Res Earth Surf 124:1201–1216. https://doi.org/10.1029/2018JF004920

Lacroix P, Berthier E, Maquerhua ET (2015) Earthquake-driven acceleration of slow-moving landslides in the Colca valley, Peru, detected from Pléiades images. Remote Sens Environ 165:148–158. https://doi.org/10.1016/j.rse.2015.05.010

Lacroix P, Bièvre G, Pathier E, Kniess U, Jongmans D (2018) Use of Sentinel-2 images for the detection of precursory motions before landslide failures. Remote Sens Environ 215:507–516. https://doi.org/10.1016/j.rse.2018.03.042

Lacroix P, Dehecq A, Taipe E (2020) Irrigation-triggered landslides in a Peruvian desert caused by modern intensive farming. Nat Geosci 13:56–60. https://doi.org/10.1038/s41561-019-0500-x

Lazecký M, Çomut FC, Hlaváčová I, Gürboğa Ş (2015) Practical application of satellite-based SAR interferometry for the detection of landslide activity. Proc Earth Planet Sci 15:613–618. https://doi.org/10.1016/j.proeps.2015.08.113

Leprince S, Barbot S, Ayoub F, Avouac J-P (2007) Automatic and precise orthorectification, coregistration, and subpixel correlation of satellite images, application to ground deformation measurements. IEEE Trans Geosci Remote Sens 45:1529–1558. https://doi.org/10.1109/TGRS.2006.888937

Locat P, Leroueil S, Locat J (2008) Remaniement et mobilité des débris de glissements de terrain dans les argiles sensibles de l'est du Canada. In: Proceedings of the 4th Canadian conference on geohazards: from causes to management. Presse de l'Université Laval, Québec, pp 97–106

Luo J, Niu F, Lin Z, Liu M, Yin G (2019) Recent acceleration of thaw slumping in permafrost terrain of Qinghai-Tibet plateau: an example from the Beiluhe Region. Geomorphology 341:79–85. https://doi.org/10.1016/j.geomorph.2019.05.020

Mackey BH, Roering JJ (2011) Sediment yield, spatial characteristics, and the long-term evolution of active earthflows determined from airborne LiDAR and historical aerial photographs, Eel River, California. GSA Bull 123:1560–1576. https://doi.org/10.1130/B30306.1

Mainsant G, Larose E, Brönnimann C, Jongmans D, Michoud C, Jaboyedoff M (2012) Ambient seismic noise monitoring of a clay landslide: toward failure prediction. J Geophys Res 117:F01030–F01030. https://doi.org/10.1029/2011JF002159

Monjuvent G (1973) La transfluence Durance-Isère. Essai de synthèse du Quaternaire du bassin du Drac (Alpes françaises). Géol Alpine 49:57–118

Moulin C, Robert Y (2004) Le glissement de l'Harmalière sur la commune de Sinard. In: Proceedings of the workshop Ryskhydrogeo, Program Interreg III, La Mure (France), 11 pp

Mulas M, Ciccarese G, Truffelli G, Corsini A (2020) Integration of digital image correlation of Sentinel-2 data and continuous GNSS for long-term slope movements monitoring in moderately rapid landslides. Remote Sens 12:2605. https://doi.org/10.3390/rs12162605

Pagano L, Picarelli L, Rianna G, Urciuoli G (2010) A simple numerical procedure for timely prediction of precipitation-induced landslides in unsaturated pyroclastic soils. Landslides 7:273–289. https://doi.org/10.1007/s10346-010-0216-x

Pazzi V, Morelli S, Fanti R (2019) A review of the advantages and limitations of geophysical investigations in landslide studies. Int J Geophys 2019:1–27. https://doi.org/10.1155/2019/2983087

Poli P (2017) Creep and slip: seismic precursors to the Nuugaatsiaq landslide (Greenland). Geophys Res Lett 44:8832–8836. https://doi.org/10.1002/2017GL075039

Renalier F, Jongmans D, Campillo M, Bard P-Y (2010) Shear wave velocity imaging of the Avignonet landslide (France) using ambient noise cross-correlation. J Geophys Res 115:F03032. https://doi.org/10.1029/2009JF001538

RESIF/OMIV (2006) National French Landslide Observatory Facility and RESIF Datacenter: French Multidisciplinary Observatory of Versant Instabilities. RESIF - Réseau Sismologique et géodésique Français. Seismic Network. https://doi.org/10.15778/RESIF.MT

Rokoengen K, Jespersen MN, Kleiv RA, Sæterbø E (2001) The 1345 slide and flood disaster in the Gauldalen valley, mid-Norway: a new interpretation. Nor Geogr Tidsskr - Nor J Geogr 55:57–70. https://doi.org/10.1080/00291950121138

Stumpf A, Malet J-P, Allemand P, Ulrich P (2014) Surface reconstruction and landslide displacement measurements with Pléiades satellite images. ISPRS J Photogramm Remote Sens 95:1–12. https://doi.org/10.1016/j.isprsjprs.2014.05.008

Stumpf A, Malet J-P, Delacourt C (2017) Correlation of satellite image time-series for the detection and monitoring of slow-moving landslides. Remote Sens Environ 189:40–55. https://doi.org/10.1016/j.rse.2016.11.007

Takasu T, Kubo N, Yasuda A (2007) A. Development, evaluation and application of RTKLIB: a program library for RTK-GPS. In Proceedings of the International Symposium on GPS/GNSS 2007, Johor Bahru, Malaysia, 5–7 November 2007; pp. 213–218

Tavenas F, Flon P, Leroueil S, Lebuis J (1983) Remolding energy and risk of slide retrogression in sensitive clays. In: Proceedings of the symposium on slopes on soft clays, linköping, sweden. SGI report. pp 423–454

Tokimatsu K (1997) Geotechnical site characterization using surface waves. Proc First Int Conf Earthq Geotech Eng 3:1333–1368

Travelletti J, Malet J-P, Samyn K et al (2013) Control of landslide retrogression by discontinuities: evidence by the integration of airborne- and ground-based geophysical information. Landslides 10:37–54. https://doi.org/10.1007/s10346-011-0310-8

Turmel D, Potvin J, Demers D, Locat P, Locat A, Locat P, Leroueil S (2018) Empirical estimation of the retrogression and the runout distance of sensitive clay flowslides. In: Proceedings of the Geohazards 7 conference, Canmore, 8 pp

Van Asch TWJ, Brinkhorst WH, Buist HJ, Vessem PV (1984) The development of landslides by retrogressive failure in varved clays. Z Geomorphol Suppl 4:165–181

van Asch TWJ, Malet J-P, Bogaard TA (2009) The effect of groundwater fluctuations on the velocity pattern of slow-moving landslides. Nat Hazards Earth Syst Sci 9:739–749. https://doi.org/10.5194/nhess-9-739-2009

Wang B, Paudel B, Li H (2009) Retrogression characteristics of landslides in fine-grained permafrost soils, Mackenzie Valley, Canada. Landslides 6(2):121–127

Wathelet M (2008) An improved neighborhood algorithm: parameter conditions and dynamic scaling. Geophys Res Lett 35:L09301. https://doi.org/10.1029/2008GL033256

Wathelet M, Guillier B, Roux P, Cornou C, Ohrnberger M (2018) Rayleigh wave three-component beamforming: signed ellipticity assessment from high-resolution frequency-wavenumber processing of ambient vibration arrays. Geophys J Int 215:507–523. https://doi.org/10.1093/gji/ggy286

Wathelet M, Jongmans D, Ohrnberger M, Bonnefoy-Claudet S (2008) Array performances for ambient vibrations on a shallow structure and consequences over Vsinversion. J Seismol 12:1–19. https://doi.org/10.1007/s10950-007-9067-x

Yamada M, Mori J, Matsushi Y (2016) Possible stick-slip behavior before the Rausu landslide inferred from repeating seismic events. Geophys Res Lett 43:9038–9044. https://doi.org/10.1002/2016GL069288

Zerathe S, Lacroix P, Jongmans D, Marino J, Taipe E, Wathelet M, Pari W, Smoll LF, Norabuena E, Guillier B, Tatard L (2016) Morphology, structure and kinematics of a rainfall controlled slow-moving Andean landslide, Peru. Earth Surf Process Landf 41:1477–1493. https://doi.org/10.1002/esp.3913

S. Fiolleau · D. Jongmans · G. Bièvre (✉) · P. Lacroix · A. Helmstetter · M. Wathelet
Univ. Grenoble Alpes, Univ. Savoie Mont Blanc, CNRS, IRD, IFSTTAR, ISTerre, 38000, Grenoble, France
Email: gregory.bievre@univ-grenoble-alpes.fr

G. Chambon
Univ. Grenoble Alpes, INRAE, UR ETNA,
Grenoble, France

M. Demierre
InfraSurvey Sarl,
Neuchâtel, Switzerland